ORIGINAL PAPER

Calibration and fast evaluation algorithms for homogeneous orthotropic polynomial yield functions

Stefan C. Soare[1] · Martin Diehl[2,3]

Abstract

Homogeneous polynomial functions have the potential to provide a general modeling framework for yield surfaces in metal plasticity. They incorporate as particular cases many of the previously proposed yield functions and their fitting capabilities allow for capturing a wide range of yield surface shapes. And yet, there are still two unsolved problems which turn into major obstacles when it comes to actual implementations in both academic and industrial environments: The lack of a general optimization algorithm for the calibration of their parameters and the lack of an efficient computational scheme for their value, gradient and hessian. The difficulty of the first problem is two-fold, necessitating an adequate specification of the experimental input data set and satisfaction of the convexity constraint. The second problem is specific to all high degree polynomials and is comprised of issues such as numerical stability, precision and implementation efficiency. We present practical solutions to both problems: An optimization algorithm that reduces to solving a sequence of quadratic problems and a double Horner evaluation scheme that is optimal (featuring the least number of multiplications). The resulting modeling framework can account for arbitrary input data, experimental or from crystal plasticity predictions. As illustration we show new results regarding the relationship between generalized r-values and the earing profile of deep-drawn cylindrical cups. Practicality is demonstrated by the high level of automation of the entire workflow, from material parameters calibration to finite element simulations, and supporting code (Python scripts and constitutive subroutine) made available at https://github.com/stefanSCS/PolyN.

1 Introduction

Phenomenological yield criteria are the essential constitutive element for the modeling of metal plasticity at continuum level [15], and for the numerical simulation of their deformation processes via the finite element method [9, 25]. To be effective, a yield criterion must be capable of fitting several stress–strain paths, which are deemed representative of the process under consideration. For sheet metal, by a long and well established tradition, these are proportional loading paths characterizing the response of the sheet to uniaxial traction along several directions, and, occasionally, to in-plane biaxial stretching. Much of the research on yield function development has been focused on functions that are capable of capturing this minimalist experimental data set as accurately as possible. Two major approaches can be distinguished based on the kind of analytical formulation employed[1]: One, using explicit homogeneous polynomial expressions of the stress components with respect to the material frame, e.g. [6, 11, 14, 15, 26], and the other, using compositions of the Hershey [13]–Hosford [17] isotropic function with linear transformations of the stress tensor to account for anisotropy, e.g., [1–4, 8, 19]. The first approach is general and transparent with respect to the number of independent material parameters, but it does not guarantee the convexity of the yield surface—this has to be enforced by the

✉ Stefan C. Soare
  stefancsoare@gmail.com

1 Technical University of Cluj-Napoca, Cluj-Napoca 400641, Romania

2 Dept. Mater. Eng., KU Leuven, Kasteelpark Arenberg 44, Leuven 3001, Belgium

3 Dept. Comp. Sci., KU Leuven, Celestijnenlaan 200 A, Leuven 3001, Belgium

---

[1] A third, is a constructive approach based on CAD-like interpolation tools [30, 38].

calibration procedure of the material parameters. On the other hand, the formulations produced by the second approach are convex functions by default, but their parameters are not guaranteed to be independent, their redundancy increasing with the number of linear transformations employed.

The development of new and advanced sheet materials, the demand for tighter and tighter tolerances in industrial design, the need for more efficient fabrication processes by reducing the energy consumption and the amounts of scrap and faulty parts—these are all factors that pose new simulation challenges and require more detailed and more accurate descriptions of mechanical properties. In general, the level of detail can be increased by enlarging the set of experiments. Since this can be an expensive endeavor when dealing with actual sheet metal, the next best alternative is provided by the so-called *virtual testing* framework, where the predictive capabilities of a crystal plasticity model of the sheet, calibrated on a small-sized experimental dataset, can be used to obtain a comprehensive description of its plastic properties, e.g., [5, 10, 24, 36, 41]. In theory, the whole yield surface could be probed and the set of (virtual) experiments enlarged arbitrarily. Then adequate modeling of large data sets requires yield functions with increased sets of material parameters.

An increased flexibility in yield surface modeling is also needed when trying to investigate and interpret experimental results. A classic example is the deep-drawing of cylindrical cups, where the relationship between the non-uniform height of the cup and the anisotropy of the sheet is still a matter of debate. The current understanding of the problem correlates the cup height profile with the response of the sheet in uniaxial tensile tests at various angles from the rolling direction [15, 18]. On the other hand, the large variety of cup profiles obtained in finite element simulations based on yield functions calibrated on uniaxial properties, e.g., [12, 28, 40], indicates that a wider zone of the yield surface—not just the curve traced on it by uniaxial tests—may be relevant for the deformation process experienced by the blank during deep-drawing. Then a rigorous investigation of the problem requires the capability of generating several distinct yield surface models of the same metal sheet, all sharing the same uniaxial properties while having tightly controlled features elsewhere. Finite element simulation will then help discern which yield surface feature, besides uniaxial properties, is most likely to have the highest impact on the cup profile.

Such modeling feats are beyond the current state-of-the-art, which is almost exclusively focused on capturing the minimalist data set discussed above. They require an optimal control of a large number of parameters and a capability of handling arbitrary data, from the traditional uniaxial tests to whole areas of the yield surface. High order homogeneous polynomials of even degree have the potential to provide a universal modeling framework for (centrally symmetric) yield functions, since they incorporate as particular cases

many of the previously proposed yield functions [27] and Appendix-E here, and their level sets are dense in the set of centrally symmetric and convex surfaces [37]. However, while theoretically appealing, there are two major problems to be tackled when trying to implement high order polynomials in practical applications. First, there is no general recipe for their parameter calibration on arbitrary data sets, with the constraint of a convex outcome; Second, if implemented in canonical form, their evaluation becomes costly and prone to precision loss as the degree increases. Previous attempts at the problem, e.g., [26, 29, 34, 39], were limited to polynomials of order ≤ 8 and, with slight variations, to the traditional data set based on uniaxial properties. In this work we propose solutions to both problems, calibration and evaluation, and based on these we develop a general modeling framework capable of handling *arbitrary* input data while ensuring convexity. The framework is then illustrated in the problem of cylindrical deep-drawing, where it is used to investigate the relationship between yield surface models and predicted cup profiles.

2 A parametrization of yield surfaces in terms of experiments

As announced in Introduction, our aim is a general modeling framework capable of handling arbitrary input data, i.e., any combination of yield stresses and directions of plastic flow. This requires a parametrization of the yield surface in terms of loading paths.

Let RD, TD and ND denote the rolling, transverse and normal directions of the sheet. These are the symmetry axes of the material (assumed orthotropic) and throughout this work the Cartesian coordinate system denoted by $Oxyz$ is aligned along these axes (Ox along RD, Oy along TD). The corresponding unit vectors will be denoted by e_x, e_y and e_z, respectively. The response of the material is assumed to be insensitive to load reversals (tension-compression symmetric).

For an angle θ measured from RD, a loading direction $u = u(\theta)$ and its orthogonal $v(\theta)$ are defined in the plane of the sheet by

$$\begin{aligned} u &= \cos\theta\, e_x + \sin\theta\, e_y \\ v &= -\sin\theta\, e_x + \cos\theta\, e_y \end{aligned} \tag{1}$$

and a sample of the sheet material is tested by subjecting it to the biaxial loading

$$\sigma = \sigma_L u \otimes u + \sigma_W v \otimes v = \sigma_L \tau \tag{2}$$

where, by defining the stress ratio $q = \sigma_W/\sigma_L$, the tensor $\boldsymbol{\tau}$ with components

$$\begin{aligned}
\tau_x &= \cos^2\theta + q\sin^2\theta \\
\tau_y &= q\cos^2\theta + \sin^2\theta \\
\tau_{xy} &= (1-q)\cos\theta\sin\theta
\end{aligned} \tag{3}$$

can be regarded as the loading direction.

For symmetry reasons it is then sufficient to consider only cases where $\sigma_x + \sigma_y \geq 0$ and $\theta \in [0, \pi/2]$. For $q = 0$ we recover the case of uniaxial loading. In general, we have $q \in [-1, 1]$. For $q = 1$ the loading reduces to balanced biaxial (for all angles θ), whereas when $q = -1$ the sample is loaded in shear: simple, when $\theta = 0$ or $\theta = \pi/2$, and pure when $\theta = \pi/4$. Thus $q \geq 0$ is representative of the stretching regime, and $q \leq 0$ of drawing. The biaxial curve (defined by $\sigma_{xy} = 0$) is generated by the two curves $\theta = 0$, $q \in [-1, 1]$, and $\theta = \pi/2$, $q \in [-1, 1]$. The entire yield surface can be parameterized by the pair (q, θ) via Eq. (2) by specifying the yielding stress $\sigma_L = \sigma_L(q, \theta)$. Illustrations are shown in Appendix-A/Figs.1,2,3-Left.

We next define the r-value of the test as the classical ratio of width to thickness strain (rates)

$$r(q, \theta) = \frac{\dot{\epsilon}_w}{\dot{\epsilon}_z} = \frac{-\nabla f \cdot \boldsymbol{v} \otimes \boldsymbol{v}}{\partial f/\partial\sigma_x + \partial f/\partial\sigma_y} \tag{4}$$

Above, ∇f denotes the gradient of the yield function and $\dot{\epsilon}_z$ was calculated via the incompressibility equation. Equation (4) extends the classical r-value to general stress states. In [35] and [28] have employed this extended definition in the context of profile predictions of deep drawn cylindrical cups. When $q = 0$ one recovers the traditional definition.

Along the biaxial curve a different deformation ratio is usually employed—the tangent of the angle of the exterior normal to one of the symmetry axes. This is easily related to the extended r-value, as defined here, by:

$$r(q, 0) = \frac{-(\partial f/\partial\sigma_y)/(\partial f/\partial\sigma_x)}{1 + (\partial f/\partial\sigma_y)/(\partial f/\partial\sigma_x)} \tag{5}$$

and by

$$r(q, \pi/2) = \frac{-(\partial f/\partial\sigma_x)/(\partial f/\partial\sigma_y)}{1 + (\partial f/\partial\sigma_x)/(\partial f/\partial\sigma_y)} \tag{6}$$

At the top of the yield surface, where $q = -1$ and $\theta = \pi/4$, the thickness strain vanishes and hence

$$\lim_{q \to -1} |r(q, \pi/4)| = +\infty$$

This infinite asymptote actually extends to the whole set of points on the yield surface defined by $\partial f/\partial\sigma_x + \partial f/\partial\sigma_y = 0$. In the case of the Von Mises function, for example, this set

is the shear curve defined by $q = -1$ and $\theta \in [0, \pi/2]$. Thus, as a characteristic common to all deformation processes involving deep-drawing, *the actual r-values featured by the material during deformation tend to deviate significantly from the ones measured from uniaxial tests as the stress state is uniaxial only at the free edges of the blank and biaxial elsewhere*.[2] Illustrations of this phenomenon for the Von Mises quadratic and models of two aluminum alloys are shown in Appendix-A/Figs.1,2,3-Right.

Equation (2) parametrizes the yield surface via the field of yield stresses along radial loading paths. In case of finite deformations, the r-values gain prominence. Equation (4) leads to the following representation of the yield surface in terms of generalized r-values:

$$\overline{\sigma}_L(q, \theta) = \overline{\sigma}_\theta \exp\left[\int_0^q \frac{r(q, \theta)\,\mathrm{d}q}{1 + (1-q)r(q, \theta)}\right] \tag{7}$$

where $\overline{\sigma}_\theta = \overline{\sigma}_L(q = 0, \theta)$ is the classical directional uniaxial yield stress. Noteworthy in the above formula (proved in Appendix-A) is that, for a fixed uniaxial curve (i.e., both classical directional stresses $\overline{\sigma}_\theta$ and r-values $r_\theta = r(q = 0, \theta)$ are fixed), the two zones of the yield surface $q < 0$ and $q > 0$ can vary, at least from a purely geometrical perspective and subject to convexity restrictions, *independently*, since they are characterized by different values of the field $r(q, \theta)$.

3 PolyN: Methodology, cost function and input data

3.1 Methodology

The yield criterion is written in the form,[3]: $P_N(\boldsymbol{\sigma}) = \overline{\sigma}^N$, where $\overline{\sigma}$ denotes the yield stress along RD. The yield function is a homogeneous polynomial P_N of even degree N—referred to as PolyN—of the stress components with respect to the $Oxyz$ frame:

---

[2] An alternative deformation ratio is $q = r/(1+r)$ (not to be confused with our usage of q), with the advantage that its variation is limited to $[0, 1]$, e.g., Ch. 10 in [20], [10]. However, the nature of the disturbance remains the same—the asymptote of the extended r-value being replaced by zeros of q.

[3] Regarding notation: Boldface symbols represent tensors/matrices; For a second order tensor/matrix $\boldsymbol{M}$ and a vector $\boldsymbol{a}$ the notation $\boldsymbol{b} = \boldsymbol{M} : \boldsymbol{a}$ stands for the component form $b_i = \sum_j M_{ij}a_j$; The scalar (dot) product of two vectors is denoted by $\boldsymbol{a} \cdot \boldsymbol{b}$; The tensor product of two vectors $\boldsymbol{a} \otimes \boldsymbol{b}$ is defined by $(\boldsymbol{a} \otimes \boldsymbol{b}) : \boldsymbol{v} = (\boldsymbol{b} \cdot \boldsymbol{v})\boldsymbol{a}$; Under plane stress conditions, a function of the stress tensor $f = f(\boldsymbol{\sigma})$ is, by virtue of the symmetry of its argument, always regarded a function $f = f(\sigma_x, \sigma_y, \sigma_{xy})$; In this condensed notation for arguments, the tensor components of the gradient are: $\nabla f = [\partial f/\partial\sigma_x, \partial f/\partial\sigma_y, (1/2)\partial f/\partial\sigma_{xy}(1/2)\partial f/\partial\sigma_{xy}]$. The summation convention on repeated indexes is not implied; Whenever used, this is stated explicitly.

$$P_N(\sigma_x, \sigma_y, \sigma_{xy}) = \sum_{i=0}^{n_m} a_i \phi_i(\sigma_x, \sigma_y, \sigma_{xy})$$

$$\phi_i(\sigma_x, \sigma_y, \sigma_{xy}) = \sigma_x^{i_1} \sigma_y^{i_2} \sigma_{xy}^{2i_3},$$

$$i_1 + i_2 + 2i_3 = N \tag{8}$$

The above analytical expression is the so-called *canonical form*, where ϕ_i are the basis functions—monomials of degree N. Orthotropic symmetry is satisfied by allowing only monomials of even degree in the shear stress component σ_{xy}. The total number of terms is then $n_m = (N/2 + 1)^2$.

When $N = 2$, Poly2 is identical to the plane stress version of [14]. Its four parameters can be related uniquely to four data points, e.g., three uniaxial stresses and one r-value, or three uniaxial r-values and one yielding stress, etc. In general, the uniaxial data is consistent with a convex shape and hence the data itself suffices to ensure the convexity of Poly2/Hill'48.

When $N = 4$, with a straightforward aggregation on the powers of σ_{xy}, we obtain Poly4:

$$P_4(\boldsymbol{\sigma}) = a_0 \sigma_x^4 + a_1 \sigma_x^3 \sigma_y + a_2 \sigma_x^2 \sigma_y^2 + a_3 \sigma_x \sigma_y^3 + a_4 \sigma_y^4$$
$$+ (a_5 \sigma_x^2 + a_6 \sigma_x \sigma_y + a_7 \sigma_y^2) \sigma_{xy}^2 + a_8 \sigma_{xy}^4$$

The nine parameters can still be related, via explicit formulas, to various combinations of nine data points selected from the more or less traditional set of uniaxial stresses and r-values augmented with balanced-biaxial and plane strain stress points, i.e., $\mathcal{S}_{exp} = \{\overline{\sigma}_{15k}, r_{15k} \mid k = 0, \ldots 6\}$ $\cup \{\overline{\sigma}_b, \overline{\sigma}_{ps0}, \overline{\sigma}_{ps90}\}$. However, this approach is in general restricted to steels, where the experimental data is conducive to a convex Poly4 shape. It no longer works for aluminum alloys, due to convexity issues. In this case, the identification strategy is usually explicit only on a subset of parameters, the rest being identified by optimization combined with some convexity check [26, 33]. Nevertheless, in both cases, the relationship between data and parameters is still one to one.

For Poly6

$$P_6(\boldsymbol{\sigma}) = a_0 \sigma_x^6 + \cdots + a_6 \sigma_y^6 + (a_7 \sigma_x^4 + \cdots + a_{11} \sigma_y^4) \sigma_{xy}^2$$
$$+ (a_{12} \sigma_x^2 + a_{13} \sigma_x \sigma_y + a_{14} \sigma_y^2) \sigma_{xy}^4 + a_{15} \sigma_{xy}^6$$

the situation changes: The data set $\mathcal{S}_{exp}$, although it has 17 data points, no longer uniquely determines the 16 parameters $a_0, \ldots, a_{15}$. More precisely, with parameters $a_0, \ldots, a_6$ calibrated on data from the plane $\sigma_{xy} = 0$, all uniaxial data in $\mathcal{S}_{exp}$ can be exactly matched by Poly6 for arbitrary values of a_{15}, [29]. In terms of the representation in Eq. (7), this means that, for a fixed uniaxial curve $q = 0$, starting with Poly6, PolyN can model the drawing zone $q < 0$ with increasing independence from the stretching zone $q > 0$, as the degree N increases, i.e., there is increased flexibility in specifying the field of generalized r-values $r(q, \theta)$. The

calibration solution adopted in the cited reference for Poly6 was to augment the mechanical data set $\mathcal{S}_{exp}$ with a set $\mathcal{S}_H$ of stress samples extracted from a small vicinity of the top point $(0, 0, \sigma_{xy})$ of an instance of Hill'48 fitted on the data points $\{\overline{\sigma}_0, \overline{\sigma}_{45}, \overline{\sigma}_{90}, r_{45}\}$. Calibration was then performed by optimizing a semi-explicit distance function on $\mathcal{S}_{exp} \cup \mathcal{S}_H$ and convexity was controlled by decreasing the weight on $\mathcal{S}_{exp}$ if not satisfied.

While simple and effective, the calibration solution devised for Poly6 is limited to the specific data set $\mathcal{S}_{exp} \cup \mathcal{S}_H$. As discussed bellow, it can be easily extended to any PolyN and can be used to construct an initial estimate of the yield surface. However, our aim here is a general calibration strategy for PolyN capable of handling arbitrary input data, so that we be able to control specific zones of the yield surface. Since we assume no a priori knowledge on whether or not the data is conducive to a convex yield surface shape, this requires a constrained optimization procedure. This was used by [26] for PolyN with $N \leq 8$, but their approach was limited to the data set $\mathcal{S}_{exp}$ and employed non-linear constraints. This type of non-linear optimization problem is notoriously difficult, especially for large scale problems, and, as noted by [34], reducing the set of constraints to obtain a more manageable problem may not ensure a convex outcome. Here we simplify considerably the optimization algorithm, while retaining generality, as follows:

- We first construct a cost function tailored on data parametrized as described in Section-2
- Then transform the non-linear optimization problem into a linearly constrained problem by using an ad-hoc constraint linearization algorithm

3.2 Cost function

For an arbitrary homogeneous polynomial of order N this has the form

$$J_N(\boldsymbol{a}) = \frac{1}{2} \sum_{j=0}^{n_d} w_j \Delta_j^2 \tag{9}$$

where n_d is the number of elements in the input dataset, w_j is the weight associated with the j-th element in the input data set, and

$$\Delta_j = \boldsymbol{a} \cdot \boldsymbol{v}_j - d_j \tag{10}$$

is the difference between the PolyN prediction, represented by the dot product $\boldsymbol{a} \cdot \boldsymbol{v}_j = \sum_{i=0}^{n_m} a_i v_{ji}$, and the data d_j. The vectors $\boldsymbol{v}_j$ are determined by the nature of their corresponding (experimental/virtual yield stress or r-value) data points and their calculation is detailed below. Before that, some straightforward manipulations obtain $\Delta_j^2 = (\boldsymbol{a} \cdot \boldsymbol{v}_j)^2 - 2\boldsymbol{a} \cdot$

$(d_j \boldsymbol{v}_j) + d_j^2 = \left[(\boldsymbol{v}_j \otimes \boldsymbol{v}_j) : \boldsymbol{a} \right] \cdot \boldsymbol{a} - \boldsymbol{a} \cdot (2 d_j \boldsymbol{v}_j) + d_j^2$, and hence the cost function is the quadratic

$$J_N(\boldsymbol{a}) = (\boldsymbol{M} : \boldsymbol{a}) \cdot \boldsymbol{a} - \boldsymbol{V} \cdot \boldsymbol{a} + D \tag{11}$$

where:

$$\boldsymbol{M} = \frac{1}{2} \sum_{j=0}^{n_d} w_j \boldsymbol{v}_j \otimes \boldsymbol{v}_j, \quad \boldsymbol{V} = \sum_{j=0}^{n_d} w_j d_j \boldsymbol{v}_j, \quad D = \frac{1}{2} \sum_{j=0}^{n_d} w_j d_j^2$$

Recalling eqs.(2) and (3), the PolyN yield surface passes through an input data point $\boldsymbol{\sigma}^{(j)} = \sigma_L^{(j)} \boldsymbol{\tau}^{(j)}$ if

$$P_N \left(\boldsymbol{\tau}^{(j)} \right) = 1/\overline{\sigma}_j^N \iff \sum_{i=0}^{n_m} a_i \phi \left(\boldsymbol{\tau}^{(j)} \right) = 1/\overline{\sigma}_j^N$$
$$\iff \boldsymbol{a} \cdot \boldsymbol{v}_j - d_j = 0 \tag{12}$$

where we denoted $\overline{\sigma}_j := \sigma_L^{(j)}/\overline{\sigma}$. Thus the relationship stating that a yield point lies on the PolyN surface is linear, of the type in Eq. (10), with the components of the vector $\boldsymbol{v}_j$ defined by $v_{ji} = \phi_i \left(\boldsymbol{\tau}^{(j)} \right)$.

By virtue of the homogeneity of PolyN, only the stress direction is relevant when specifying r-values. Then using Eq. (4), the PolyN surface has the r-value r_j along a loading direction $\boldsymbol{\tau}^{(j)}$ if

$$\boldsymbol{a} \cdot \boldsymbol{v}_j = 0 \tag{13}$$

where

$$v_{ji} = \left(r_j + \sin^2 \theta_j \right) \frac{\partial \phi_i}{\partial \sigma_x} \left(\boldsymbol{\tau}^{(j)} \right) + \left(r_j + \cos^2 \theta_j \right) \frac{\partial \phi_i}{\partial \sigma_y} \left(\boldsymbol{\tau}^{(j)} \right) - \cos \theta_j \sin \theta_j \frac{\partial \phi_i}{\partial \sigma_{xy}} \left(\boldsymbol{\tau}^{(j)} \right)$$

3.3 Input data and weights

The minimal data set we consider consists of 16 data points[4]: the yield stresses $\{ \overline{\sigma}_{\theta_k} \}$ and r-values $\{ r_{\theta_k} \}$ corresponding to uniaxial tests on samples cut from the sheet at angles $\theta_k = 15^o k$ from RD, with $k = 0, \dots, 6$; and the balanced-biaxial yield stress $\overline{\sigma}_b$ and r-value r_b. In terms of the (q, θ) parameters these data points are described by: $\overline{\sigma}_L(q = 0, \theta = \theta_k) = \overline{\sigma}_{\theta_k}$, $r(q = 0, \theta = \theta_k) = r_{\theta_k}$, with $k = 0, \dots, 6$, and balanced-biaxial $\overline{\sigma}_L(q = 1, \theta = 0) = \overline{\sigma}_b$, $r(q = 1, \theta = 0) = -r_b/(1 + r_b)$. We recall that the hardening curve is defined by the tensile test along RD and hence $\overline{\sigma} = \sigma_0 \iff \overline{\sigma}_0 = 1$.

The above data set is enhanced by adding any supplementary information about the yield surface. Concrete examples

---

[4] This requirement can be easily relaxed to 7 data points by interpolating the uniaxial data.

will be featured in later sections. More generally, we consider input data sets of the form parametrized by Eq. (2):

$$\{ \overline{\sigma}_L(q = q_{j_1}, \theta = \theta_{j_2}) \} \bigcup \{ r(q = q_{j_1}, \theta = \theta_{j_2}) \}$$

In cases where no information is available other than the minimal data set, the linear system solving the least squares problem associated with the cost function in Eq. (11) becomes under-determined. We solve this problem by augmenting the minimal data set with a set $\mathcal{S}_H$ of samples extracted from the top of an instance of Hill'48 calibrated as discussed above.

We refer to a data point as *actual* if it originates in an actual experiment and as *virtual* if it originates from a numerically simulated experiment (based on crystal plasticity). Since we use weights to emphasize more/less the contribution of actual/virtual data points, the terminology can be extended to more/less *important* data points. This can be used to guide a PolyN model towards a better fit of some specific points. Then we assign overall weights $W_A \in (0, 1]$ and $W_V \in [0, 1)$ to the whole subsets of actual and virtual data points, respectively, such that $W_A + W_V = 1.0$. The overall weights W_A and W_V are then redistributed uniformly with different weight fractions over the yield stresses and r-values of each subset in a manner entirely similar to that described in [30].

4 PolyN: convexity constraints and optimization algorithm

4.1 General considerations: quadratic constraints

As discussed in Methodology, our PolyN calibration strategy requires a constrained optimization procedure in order to enforce convexity. Two lemmas are of considerable help in this problem, [27]: (1) The set of parameters for which PolyN is convex is convex; (2) A PolyN level surface is convex if and only if for any plane section passing through the origin of the ambient space there holds

$$N g_N^2 - \left(1 - \frac{1}{N} \right) \left(\frac{\mathrm{d} g_N}{\mathrm{d}\omega} \right)^2 + g_N \frac{\mathrm{d}^2 g_N}{\mathrm{d}\omega^2} \geq 0 \tag{14}$$

where $\omega \in [0, 2\pi)$ is the angular parameter of the polar coordinate system in the plane section and $g_N(\omega)$ denotes the restriction of P_N to the unit circle of the section. As shown below, the above inequality results, in general, in a quadratic constraint for the parameters of PolyN. Hence the feasible set of parameters is described by non-linear inequalities, rendering the optimization problem itself nonlinear. Since the set of constraints that need be enforced in practice is quite large, this becomes a medium-to-large scale nonlinear programming problem. This class of problems is in general hard to

solve and, more relevant to us, less amenable to automation. However, because of Lemma 1 above, the feasibility domain of our problem can be approximated by *linear* constraints, a simplification that will allow us to transform it into a classical quadratic programming problem.

We next detail the reformulation of Eq. (14) in terms of PolyN parameters $\boldsymbol{a} = [a_0, a_1, \ldots, a_{n_m}]^T$. From now on, we regard the stress tensor as a vector $[\sigma_x, \sigma_y, \sigma_{xy}]^T$. Let $\{\boldsymbol{e}_1, \boldsymbol{e}_2, \boldsymbol{e}_3\}$ (re)denote the orthonormal frame aligned with the symmetry axes RD, TD and ND, respectively, and let $\{\widehat{\boldsymbol{e}}_1, \widehat{\boldsymbol{e}}_2, \widehat{\boldsymbol{e}}_3\}$ denote an arbitrary orthonormal frame of the same orientation as $\{\boldsymbol{e}_i\}$. The plane $\Pi(\widehat{\boldsymbol{e}}_3)$ determined by the linear span of $\widehat{\boldsymbol{e}}_1$ and $\widehat{\boldsymbol{e}}_2$ is then an arbitrary plane (of unit normal $\widehat{\boldsymbol{e}}_3$) passing through the origin. The unit circle of $\Pi(\widehat{\boldsymbol{e}}_3)$ is described by $\boldsymbol{\sigma} = \cos(\omega)\widehat{\boldsymbol{e}}_1 + \sin(\omega)\widehat{\boldsymbol{e}}_2$. Letting $\boldsymbol{R} = [R_{ij}]$ denote the rotation that relates $\{\widehat{\boldsymbol{e}}_i\}$ to $\{\boldsymbol{e}_j\}$ we have $\widehat{\boldsymbol{e}}_1 = R_{i1}\boldsymbol{e}_i$ and $\widehat{\boldsymbol{e}}_2 = R_{i2}\boldsymbol{e}_i$ (summation implied) and hence the unit circle with respect to the symmetry frame reads

$$\boldsymbol{\sigma}(\omega) = \begin{bmatrix} \sigma_x(\omega) \\ \sigma_y(\omega) \\ \sigma_{xy}(\omega) \end{bmatrix} = \begin{bmatrix} R_{11}\cos\omega + R_{12}\sin\omega \\ R_{21}\cos\omega + R_{22}\sin\omega \\ R_{31}\cos\omega + R_{32}\sin\omega \end{bmatrix} \quad (15)$$

The restriction of P_N to the unit circle of $\Pi(\widehat{\boldsymbol{e}}_3)$ and its derivatives are then

$$g_N(\omega) = \sum_{i=0}^{n_m} a_i \phi_i(\boldsymbol{\sigma}(\omega)) = \boldsymbol{a} \cdot \boldsymbol{\alpha}(\omega)$$
$$\frac{\mathrm{d}g_N}{\mathrm{d}\omega} = \sum_{i=0}^{n_m} a_i \frac{\mathrm{d}\phi_i}{\mathrm{d}\omega}(\boldsymbol{\sigma}(\omega)) = \boldsymbol{a} \cdot \boldsymbol{\beta}(\omega) \quad (16)$$
$$\frac{\mathrm{d}^2 g_N}{\mathrm{d}\omega^2} = \sum_{i=0}^{n_m} a_i \frac{\mathrm{d}^2\phi_i}{\mathrm{d}\omega^2}(\boldsymbol{\sigma}(\omega)) = \boldsymbol{a} \cdot \boldsymbol{\gamma}(\omega)$$

where the components of the $\boldsymbol{\alpha}$, $\boldsymbol{\beta}$ and $\boldsymbol{\gamma}$ vectors are given by:

$$\alpha_i(\omega) = \phi_i(\sigma_x(\omega), \sigma_y(\omega), \sigma_{xy}(\omega))$$
$$\beta_i(\omega) = \frac{\mathrm{d}\phi_i}{\mathrm{d}\omega}(\sigma_x(\omega), \sigma_y(\omega), \sigma_{xy}(\omega)) \quad (17)$$
$$\gamma_i(\omega) = \frac{\mathrm{d}^2\phi_i}{\mathrm{d}\omega^2}(\sigma_x(\omega), \sigma_y(\omega), \sigma_{xy}(\omega))$$

Substituting into Eq. (14) obtains, after some straightforward manipulations, the quadratic inequality

$$(\boldsymbol{Q} : \boldsymbol{a}) \cdot \boldsymbol{a} \geq 0 \quad (18)$$

where

$$\boldsymbol{Q} = N\boldsymbol{\alpha} \otimes \boldsymbol{\alpha} - \left(1 - \frac{1}{N}\right)\boldsymbol{\beta} \otimes \boldsymbol{\beta} + \frac{1}{2}(\boldsymbol{\alpha} \otimes \boldsymbol{\gamma} + \boldsymbol{\gamma} \otimes \boldsymbol{\alpha})$$

4.2 Constructing a set of quadratic constraints

In a numerical implementation the constraints are enforced at a discrete set of points on the unit sphere of the stress space, parameterized by coordinates $\theta \in [0, \pi/2]$ and $\phi \in [0, 2\pi)$ (to save notation, we continue to use θ and ϕ but with no relationship to usage in previous or later sections):

$$\sigma_{xy} = \cos\theta, \quad \sigma_y = \sin\theta\sin\phi, \quad \sigma_x = \sin\theta\cos\phi$$

To ensure a proper covering of the unit sphere we follow an approach similar to that employed by [30] and consider a quasi-uniform distribution of points $\{\boldsymbol{p}_{ij} = (\theta_i, \phi_j)\}$ on the half top of the unit sphere. The tangent space at a generic point $\boldsymbol{p} = (\theta, \phi)$ not at the north pole is generated by

$$\boldsymbol{u}_\theta = \frac{\partial\boldsymbol{\sigma}}{\partial\theta} = \cos\theta\cos\phi\boldsymbol{e}_1 + \cos\theta\sin\phi\boldsymbol{e}_2 - \sin\theta\boldsymbol{e}_3$$
$$\boldsymbol{u}_\phi = \frac{\partial\boldsymbol{\sigma}}{\partial\theta} = -\sin\theta\sin\phi\boldsymbol{e}_1 + \sin\theta\cos\phi\boldsymbol{e}_2$$

while at the north pole a basis of the tangent space is $\{\boldsymbol{e}_1, \boldsymbol{e}_2\}$.

In the tangent space at a generic point $\boldsymbol{p}$ we consider a set of n_t tangent directions

$$\boldsymbol{v}(\psi_k) = \cos\psi_k\boldsymbol{u}_\phi + \sin\psi_k\boldsymbol{u}_\theta \quad (19)$$

where $\psi_k = 2k\pi/n_t$, and $k = 0, 1, .., n_t - 1$. The position vector $\boldsymbol{\sigma}$ of point $\boldsymbol{p}$ together with a tangent vector $\boldsymbol{v}$ then determine a plane section $\Pi(\boldsymbol{\sigma} \times \boldsymbol{v})$ whose unit circle is parametrized by Eq. (15). On this circle, point $\boldsymbol{p}$ corresponds to $\omega = 0$ and the relevant components of the rotation matrix (where $\boldsymbol{\sigma}$ plays the role of $\widehat{\boldsymbol{e}}_1$) are $R_{11} = (\widehat{\boldsymbol{e}}_1)_1 = \sigma_x$, $R_{21} = (\widehat{\boldsymbol{e}}_1)_2 = \sigma_y$, and $R_{31} = (\widehat{\boldsymbol{e}}_1)_3 = \sigma_{xy}$.

The quadratic constraint in Eq. (18) is enforced for each plane section $\Pi(\boldsymbol{\sigma} \times \boldsymbol{v})$ at point $\boldsymbol{p}$ only. Thus $\omega = 0$ and further

$$\left.\frac{\mathrm{d}\boldsymbol{\sigma}}{\mathrm{d}\omega}\right|_{\omega=0} = \boldsymbol{v}, \quad \left.\frac{\mathrm{d}^2\boldsymbol{\sigma}}{\mathrm{d}\omega^2}\right|_{\omega=0} = -\boldsymbol{\sigma}$$

formulas which, together with Eq. (16), complete our definition of the set of constraints.

4.3 Constraint linearization and optimization algorithm

Let $\mathcal{S} = \{\boldsymbol{Q}_p \mid p = 1, \ldots, n_Q\}$ denote the set of $n_m \times n_m$ matrices defining the set of constraints, where each $\boldsymbol{Q}_p$ in the set corresponds to a point $\boldsymbol{\sigma}$ on the unit sphere of the stress space and to a tangent direction $\boldsymbol{v}$ as defined in the previous two subsections. Our problem consists in solving

$$\begin{cases} \min_{\boldsymbol{a} \in \mathbb{R}^{n_m}} J_N(\boldsymbol{a}) \\ \text{subject to: } (\boldsymbol{Q} : \boldsymbol{a}) \cdot \boldsymbol{a} \geq 0, \ \forall \boldsymbol{Q} \in \mathcal{S} \end{cases} \qquad (20)$$

with J_N defined by Eq. (11). We seek a solution iteratively as follows.

In the first step we solve the unconstrained least squares problem $\min J_N(\boldsymbol{a})$. If the underlying linear system is determined (in a least-square sense), a unique solution $\boldsymbol{a}_1$ exists. We check if it satisfies the set of constraints $\mathcal{S}$. If it does, the algorithm stops and $\boldsymbol{a}_1$ is accepted as solution. In general, this happens only if the data is conducive to a convex solution. In essence, this is the Poly2(Hill'48)-like, explicit solution discussed in the introductory paragraph of Section-3.

If not all the constraints in $\mathcal{S}$ are satisfied, then in the second step we let $\mathcal{P}_1$ denote the subset of indexes identifying the constraints violated by $\boldsymbol{a}_1$:

$$\mathcal{P}_1 = \left\{ p \in \{1, \ldots, n_Q\} \mid (\boldsymbol{Q}_p : \boldsymbol{a}_1) \cdot \boldsymbol{a}_1 < 0 \right\}$$

For each quadratic constraint associated with a matrix $\boldsymbol{Q}_p$ with $p \in \mathcal{P}_1$ we construct a linear substitute as follows. We let $\mathcal{K}$ denote the set of all parameters for which P_N is convex. $\mathcal{K}$ itself is convex and is contained within the feasibility domain of problem (20). Next, we denote by M the Von Mises point[5] in the space of parameters of PolyN. Then P_N with parameters M is convex and hence $M \in \mathcal{K}$. More precisely, M is within the (topological) interior of $\mathcal{K}$. Since for an index $p \in \mathcal{P}_1$ we have $(\boldsymbol{Q}_p : \boldsymbol{a}_1) \cdot \boldsymbol{a}_1 < 0$, the two points $\boldsymbol{a}_1$ and M are strictly separated by the conic surface $s_p(\boldsymbol{a}) = (\boldsymbol{Q}_p : \boldsymbol{a}) \cdot \boldsymbol{a} = 0$,

and hence the open segment $(\boldsymbol{a}_1, M)$ intersects it at a unique point

$$\boldsymbol{c}_p = M + \lambda_p \boldsymbol{u}_1, \quad \text{with } \boldsymbol{u}_1 = \boldsymbol{a}_1 - M$$

The scalar λ_p is determined from the quadratic equation $s_p(\boldsymbol{c}_p) = 0$ based on the condition that $0 < \lambda_p < 1$:

$$\lambda_p = \frac{\beta + \sqrt{\Delta}}{-\alpha}$$

where $\beta = (\boldsymbol{Q}_p : M) \cdot \boldsymbol{u}_1$, $\alpha = (\boldsymbol{Q}_p : \boldsymbol{u}_1) \cdot \boldsymbol{u}_1$, $\gamma = (\boldsymbol{Q}_p : M) \cdot M$ and $\Delta = \beta^2 - \alpha \gamma$. With point $\boldsymbol{c}_p$ determined, we construct the linear constraint defining the half-space on the positive side of the hyper-plane that passes through $\boldsymbol{c}_p$ and is tangent at the conic surface $s_p(\boldsymbol{a}) = 0$:

$$(\boldsymbol{a} - \boldsymbol{c}_p) \cdot \nabla s_p(\boldsymbol{c}_p) \geq 0$$

---

[5] For any even integer $N \geq 2$, there exists a unique set of coefficients denoted by $\boldsymbol{a} = M$ that reduces PolyN to the Von Mises yield function. These are found by reducing to identity the equality $P_N(\boldsymbol{\sigma}) = \left(\sigma_x^2 - \sigma_x \sigma_y + \sigma_y^2 + 3\sigma_{xy}^2 \right)^{(N/2)}$, with P_N defined in Eq. (8).
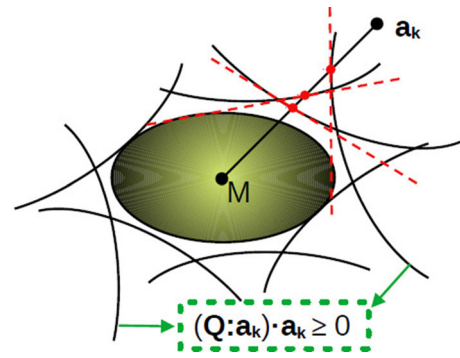
Fig. 1 Illustration of the constraint selection and linearization procedures used by the optimization algorithm. The black continuous lines show the quadratic constraints and the shaded oval represents the convexity domain of PolyN—the intersection of all constraints. The point M at its center represent the Von Mises PolyN-parameters. Point $\boldsymbol{a}_k$ represents a solution at iteration k not satisfying the entire set of quadratic constraints. All violated constraints are replaced by their tangents (red dashed lines) at the intersection points (red dots) with the segment joining $\boldsymbol{a}_k$ to M. (Color figure online)

which is equivalent to $(\boldsymbol{Q}_p : \boldsymbol{c}_p) \cdot \boldsymbol{a} \geq (\boldsymbol{Q}_p : \boldsymbol{c}_p) \cdot \boldsymbol{c}_p$, and further to:

$$\boldsymbol{h}_p \cdot \boldsymbol{a} - \zeta_p \geq 0$$

where $\boldsymbol{h}_p = \boldsymbol{Q}_p : \boldsymbol{c}_p$ and $\zeta_p = (\boldsymbol{Q}_p : \boldsymbol{c}_p) \cdot \boldsymbol{c}_p$. A schematics of this construction is shown in Fig. 1.

We then solve the quadratic problem

$$\begin{cases} \min_{\boldsymbol{a} \in \mathbb{R}^{n_m}} J_N(\boldsymbol{a}) \\ \text{subject to: } \boldsymbol{h}_p \cdot \boldsymbol{a} - \zeta_p \geq 0, \ \forall p \in \mathcal{P}_1 \end{cases} \qquad (21)$$

Its solution $\boldsymbol{a}_2$ is checked for satisfaction of all the constraints in $\mathcal{S}$. If the subset

$$\mathcal{P}_2 = \left\{ p \in \{1, \ldots, n_Q\} \mid (\boldsymbol{Q}_p : \boldsymbol{a}_2) \cdot \boldsymbol{a}_2 < 0 \right\}$$

is not empty, then the above construction of linear constraints is repeated for $\mathcal{P}_2$ and at the third iteration we solve

$$\begin{cases} \min_{\boldsymbol{a} \in \mathbb{R}^{n_m}} J_N(\boldsymbol{a}) \\ \text{subject to: } \boldsymbol{h}_p \cdot \boldsymbol{a} - \zeta_p \geq 0, \ \forall p \in \mathcal{P}_1 \bigcup \mathcal{P}_2 \end{cases} \qquad (22)$$

The sequence of iterations continues until one of the following stopping criteria is met: (1) All constraints in $\mathcal{S}$ are satisfied; (2) Or the distance between two consecutive solutions becomes less than a specified tolerance: $|\boldsymbol{a}_{k+1} - \boldsymbol{a}_k| < \epsilon$; (3) Or a specified maximum number of iterations has been reached.

We close this section with some implementation notes:

- In practice, we split the calibration procedure in two steps: We first identify all parameters $a_0, \ldots, a_N$ asso-

ciated with the biaxial curve $\sigma_{xy} = 0$, and then, with these fixed, we calibrate the rest of the parameters a_i, $i = N + 1, \ldots, n_m$.

- The calibration of the biaxial parameters $a_0, \ldots, a_N$ uses a Bezier5YS guide curve constructed from the input data [30].
- Quadratic constraints are constructed at the 9960 locations of a quasi-uniform grid on the half top of the unit sphere, each with 72 tangent directions, amounting to a total of about 7×10^5 constraints. The number of accumulated violated constraints during a sequence of iterations is much smaller than the total number of constraints—of the order of $10^3 - 10^4$, in general. Thus the corresponding quadratic problem is actually a small-to-medium sized problem.
- The quadratic problems are solved using the cvxopt optimization library [7].
- In case the optimization algorithm has found a solution satisfying all the quadratic constraints (stopping criterion 1), the convexity of the solution is again verified by evaluating the principal minors of the hessian of P_N and the Gaussian curvature of the yield surface on a dense cloud of random and regular grid points on the unit sphere consisting of about 10^5 points, by a procedure similar to [30].

5 Computational algorithm for yield function values, gradient and hessian

5.1 General considerations

At constitutive level we assume that the flow rule is *associate*, e.g., [16] and [23], and use the simplest rate independent model:

$$
\begin{aligned}
&\boldsymbol{\sigma} + \boldsymbol{\sigma W} - \boldsymbol{W\sigma} = \boldsymbol{C} : \left[\boldsymbol{D} - \boldsymbol{D}^p\right] \\
&\boldsymbol{D}^p = \bar{\epsilon}^p \frac{\partial f}{\partial \boldsymbol{\sigma}} \\
&\mathcal{F}(\boldsymbol{\sigma}, \bar{\epsilon}^p) = f(\boldsymbol{\sigma}) - H(\bar{\epsilon}^p) \leq 0 \\
&\bar{\epsilon}^p \geq 0, \ \bar{\epsilon}^p \mathcal{F} = 0
\end{aligned}
\tag{23}
$$

where $\boldsymbol{\sigma}$ is the Cauchy stress, $\boldsymbol{D}$ the rate of deformation tensor, $\boldsymbol{W}$ the skew part of the spatial velocity gradient, and $\boldsymbol{C}$ is the constant fourth order tensor of isotropic elasticity. The tensor $\boldsymbol{D}^p$ is the plastic strain rate, $\mathcal{F}$ is the yield criterion, f is the yield function (assumed to be convex and positive first order homogeneous), $H = H(\bar{\epsilon}^p)$ is the hardening curve of a uniaxial traction test, and $\bar{\epsilon}^p$ is a (scalar) measure of the accumulated plastic strain, describing the isotropic expansion of the yield surface $\mathcal{F} = 0$ as the plastic straining progresses. This is the simplest model of hardening, referred to as isotropic hardening. Thus, in this constitutive model,

the yield function is the central element and its impact upon the overall deformation can be easily discerned.

Implicit FE-codes solve the discretized equations of motion via the Newton-Raphson algorithm. This requires the constitutive response at integration points. Specifically, given the state $\left\{\boldsymbol{\sigma}_n, \bar{\epsilon}_n^p\right\}$ at time t_n, and a strain increment $\Delta\boldsymbol{\epsilon}$ supposed to advance the solution at time t_{n+1}, one has to calculate the new state $\left\{\boldsymbol{\sigma}_{n+1}, \bar{\epsilon}_{n+1}^p\right\}$. This is achieved by numerically integrating the coupled o.d.e.-algebraic system in Eq. (23). Its discretization based on the backward Euler-scheme, and the solution of the resulting algebraic system via Newton-Raphson leads to the standard return mapping algorithm, [25]. Its adaptation to plane stress, enhanced with a simple quadratic line search (based on initial slope and the start-end values of a Newton increment) was implemented as UMAT subroutine and used in all Abaqus/Standard (implicit) simulations reported in this work.

5.2 Double Horner evaluation scheme

The efficiency of the return mapping algorithm depends significantly on that of the evaluation of the yield function, its gradient and hessian. The objective here is the design of an efficient evaluation scheme for plane stress orthotropic homogeneous polynomials of arbitrary order (degree). For this purpose, we rewrite PolyN, the orthotropic homogeneous polynomial of degree N in the variables σ_x, σ_y and σ_{xy}, in the form

$$
P_N = \sum_{k=0}^{N/2} R_{N-2k}(\sigma_x, \sigma_y)\sigma_{xy}^{2k}
\tag{24}
$$

where R_{N-2k} is a homogeneous polynomial of degree $N-2k$ in the variables σ_x and σ_y:

$$
R_{N-2k} = \sum_{j=0}^{N-2k} a_j^k \sigma_x^{N-2k-j} \sigma_y^{j}
\tag{25}
$$

In the last equation, for a more concise notation, the polynomial coefficients a_k have been double-indexed according to the rule

$$
\begin{aligned}
&a_0^0 = a_0, \ a_1^0 = a_1, \ \ldots, \ a_N^0 = a_N, \\
&a_0^1 = a_{N+1}, \ a_1^1 = a_{N+2}, \ \ldots, \\
&a_{N-1}^1 = a_{2N-1}, \ \ldots, \ a_0^{N/2} = a_{N_C}
\end{aligned}
\tag{26}
$$

where, recall, $N_C = (1 + N/2)^2$ denotes the total number of parameters (coefficients) of P_N.

In what follow we assume that either $\sigma_x \neq 0$ or $\sigma_y \neq 0$ (within some given small tolerance), for otherwise the stress tensor is considered to be a simple shear, and define the ratios ρ and γ, and the multiplier t by
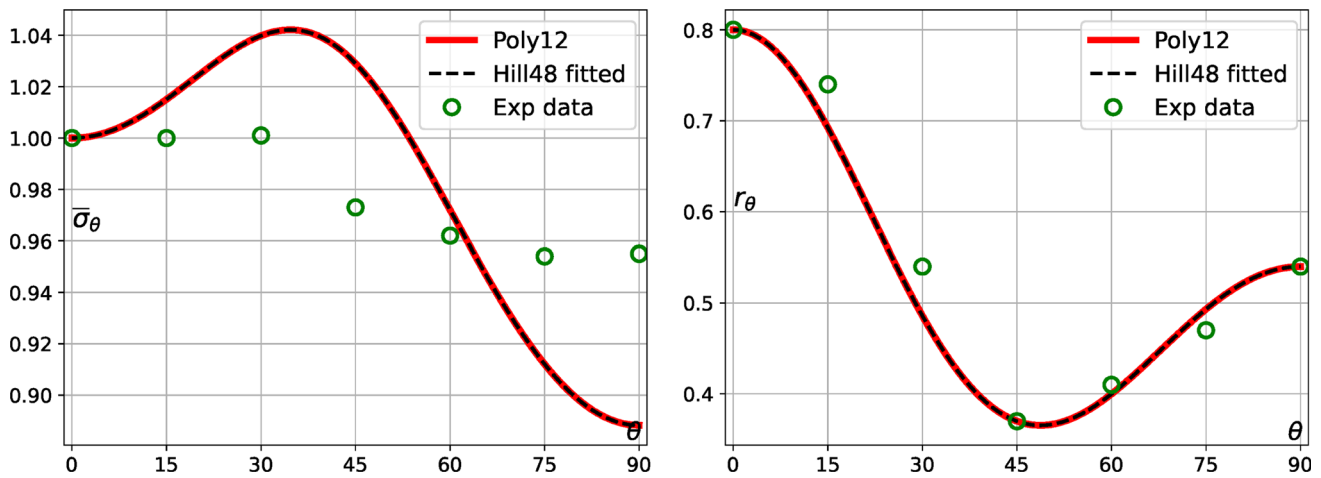
Fig. 2 Hill'48 model (of AA6022-T4) and its Poly12 replica (clone): yield stresses and r-values

$$\rho = \begin{cases} \sigma_y/\sigma_x, & \text{if } |\sigma_x| \geq |\sigma_y| \\ \sigma_x/\sigma_y, & \text{if } |\sigma_x| < |\sigma_y| \end{cases}, \quad \gamma = \left(\frac{\sigma_{xy}}{t}\right)^2 \quad (27)$$

$$t = \begin{cases} \sigma_x, & \text{if } |\sigma_x| \geq |\sigma_y| \\ \sigma_y, & \text{if } |\sigma_x| < |\sigma_y| \end{cases} \quad (28)$$

In particular, the ratio ρ is always within the interval $[-1, +1]$. We shall also need to retain a sequence of values of R_{N-2k} which is recorded as

$$b_k = \begin{cases} R_{N-2k}(1, \rho), & \text{if } |\sigma_x| \geq |\sigma_y| \\ R_{N-2k}(\rho, 1), & \text{if } |\sigma_x| < |\sigma_y| \end{cases} \quad (29)$$

where $k = 0, \ldots, N/2$. We observe that if we refine the indexing scheme in Eq. (26) by allowing it to reverse its order depending on whether or not $|\sigma_x| \geq |\sigma_y|$, i.e., the indexing in Eq. (26) is employed for the case $|\sigma_x| \geq |\sigma_y|$, and the reversed

$$a_0^0 = a_N, \ a_1^0 = a_{N-1}, \ \ldots, \ a_{N-1}^0 = a_1, \ a_N^0 = a_0$$
$$a_0^1 = a_{2N-1}, \ a_1^1 = a_{2N-2}, \ \ldots, \ a_{N-1}^1 = a_{N+1},$$
$$\ldots, \ a_0^{N/2} = a_{N_C}$$

when $|\sigma_x| < |\sigma_y|$, then the definition of b_k is reduced to the single formula

$$b_k = a_0^k + a_1^k \rho + \cdots + a_{N-2k}^k \rho^{N-2k} =$$
$$a_0^k + \rho(a_1^k + \rho(a_2^k + \cdots + \rho(a_{N-2k-1}^k + \rho a_{N-2k}^k) \ldots)) \quad (30)$$

The second equality in the above formula is meant to indicate the Horner-scheme by which b_k is actually computed in practice. Then

$$P_N = t^N Y_f \quad (31)$$

where

$$Y_f = \sum_{k=0}^{N/2} b_k \gamma^k = b_0 + \gamma(b_1 + \gamma(b_2 \ldots \\ + \gamma(b_{N/2-1} + \gamma b_{N/2}) \ldots)$$

where the second equality in the definition of Y_f indicates again the Horner-scheme used to evaluate it. We note that the only power that needs to be calculated is that involved in the final evaluation of the yield function value:

$$f(\sigma_x, \sigma_y, \sigma_{xy}) = P_N^{1/N} = |t| Y_f^{1/N} \quad (32)$$

Thus f is evaluated via two nested Horner sequences: The inner one is on the polynomial multipliers R_{N-2k}, and the other on the powers of the shear component. The evaluation scheme for gradient and hessian employs similar developments which are detailed in Appendix-B.

6 Validation and performance evaluation

6.1 Simulation of uniaxial tests

In order to discern as clearly as possible the impact of numerical evaluations of a PolyN model (yield function values, gradient and hessian) upon the overall run time of a finite element simulation we use the fact that any P_N can replicate the Hill'48 model identically. Then our evaluation methodology is as follows. First, we construct a Hill'48 model of AA6022T4 based on the dataset $\{\bar{\sigma}_0, r_0, r_{45}, r_{90}\}$ and simulate uniaxial tensile and cup-drawing tests using the default Abaqus implementation of Hill'48. Then we redo the same simulations but this time with UMAT implementing Hill'48 (in classic, quadratic form). This will allow us to test the
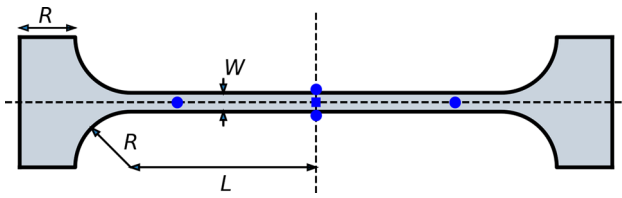
Fig. 3 Uniaxial sample used in simulations: Shape and dimensions ($R = 3W$, $L = 10W$); Dashed lines show the global (spatial) reference axes for the motion simulated in Abaqus: x-axis is horizontal, y-axis is vertical; The square marker (at the center) indicates the location of the element where FE-calculated strains are sampled; The two circle markers ($\approx 3L/4$ from center) on the x-axis indicate the location of the nodes where FE-calculated horizontal displacements are sampled; The two circle markers ($W/2$ from center) on the y-axis indicate the locations where vertical displacements are sampled

correctness of the UMAT implementation and also to evaluate its raw performance—the implementation of the return mapping algorithm itself. Finally, in the third testing step, we perform again the same simulations, this time using PolyN replicas of Hill'48 as yield functions, for $N = 4, 6, 8, 10, 12$. The Hill'48 model, overlapped with its Poly12 clone is illustrated in Fig. 2.

We simulate the uniaxial traction test of a rectangular piece of sheet metal cut from the sheet at various angles from the rolling direction: 0°, 15°, 30°, 45°, 60°, 75°, and 90°. The sample setup is shown in Fig. 3. All samples were subject to the same elongation (enforced as a displacement boundary condition), resulting in roughly 20% longitudinal strain (with plus/minus variations depending on the testing angle). We used elasticity parameters $E = 70$(GPa) and $\nu = 0.33$, and the hardening law reported for this material in [32]—the Voce exponential function: $H(\bar{\epsilon}) = A - B \exp(-C\bar{\epsilon})$, $A = 436.0$(MPa), $B = 222.0$(MPa), $C = 6.75$. A typical result is shown in Fig 4. The corresponding r-value is calculated from a simulation by two methods: First, by directly recording the strain reported by Abaqus at the center element depicted in Fig. 3, and second, by calculating the strains from the displacements sampled at the nodes in Fig. 3 with:

$$\epsilon_{11} = \ln\left(\frac{|N_1 N_2|}{|N_1^0 N_2^0|}\right), \quad \epsilon_{22} = \ln\left(\frac{|N_3 N_4|}{|N_3^0 N_4^0|}\right)$$

where $N_1^0 N_2^0$ and $N_1 N_2$ denote the line segments between the two sampling nodes on the x-axis in the reference (initial) and deformed configurations, respectively, and similarly for the segments $N_3^0 N_4^0$ and $N_3^0 N_4^0$ on the y-axis. As reflected in Fig. 4, the strains inferred from nodes are slightly less accurate by comparison with the element strains (this is expected, since strains at nodes are interpolated from those at integration points). These inferred strains are more important to us since later (for cup-drawing tests) we measure dimensions directly on the deformed geometry. Table 1 shows a performance summary of the tests. The overall run-times are

similar, with less than 3% increase from Poly4 to Poly12. Accuracy also is the same for all test cases: There is no precision loss between Hill'48 to Poly12. The largest error with respect to the theoretical expected value is attained for the 60°-test, a case further detailed in Fig. 5.

6.2 Simulation of cup-drawing

We next show the corresponding results for cup-drawing simulations. The setup is shown in Fig. 6 with specifics taken from [32]:

$$\begin{aligned} \Phi_D &= 102.11, \ \Phi_P = 100.0, \ R_N = 12.0, \\ R_S &= 6.0, \ \Phi_B = 170.0, \ h_H = 1.04, \\ t_B &= 1.0, \ \mu = 0.22 \end{aligned} \tag{33}$$

where all dimensions are in mm and Φ_B, h_H, t_B and μ represent, respectively: blank diameter, (fixed) holder clearance, blank thickness and friction coefficient. For all simulations we used *soft* contact (finite sliding, no sticking) with exponential pressure-overclosure relationship defined by: zero pressure distance = 0.001(mm) for all three tools, contact pressure = $s_T \sigma_0$, where σ_0 is the yield stress along RD, and the scaling factor $s_T = 0.1, 0.1, 0.5$, for Holder-Blank, Die-Blank and Punch-Blank interactions, respectively.

Given the symmetry of the problem, only a quarter of the blank was simulated. The results for Hill'48 are shown in Fig. 7. Thickness effects were not considered and hence for all simulations reported here the cup height profile was calculated as $H(\theta) = t_B + z(p_\theta) - z_C$, where p_θ is a node on the top of the cup, $z(p_\theta)$ is its z-coordinate, and z_C the z-coordinate of the center node at the bottom of the cup (both coordinates extracted at the end of a simulation). In order to asses the precision loss of the PolyN evaluation scheme we measure the Euclidean distance between two profiles

$$\Delta_H = \left\{ \sum_\theta [H(\theta) - H_R(\theta)]^2 \right\}^{1/2} \tag{34}$$

with H_R being a reference profile. The results are recorded in Table 2.

● Preliminary conclusions
Based on the results reported in this section, we may conclude that for PolyN with $N \leq 12$:

– The precision loss due to the evaluation of PolyN is negligible. The r-values predicted by FE-simulations of uniaxial tests feature an error limited to at most the third decimal place at integration points, and to the second at nodes. This is further confirmed by cup-drawing simulations, where differences between the profiles predicted by PolyN replicas of the same model are limited to at most
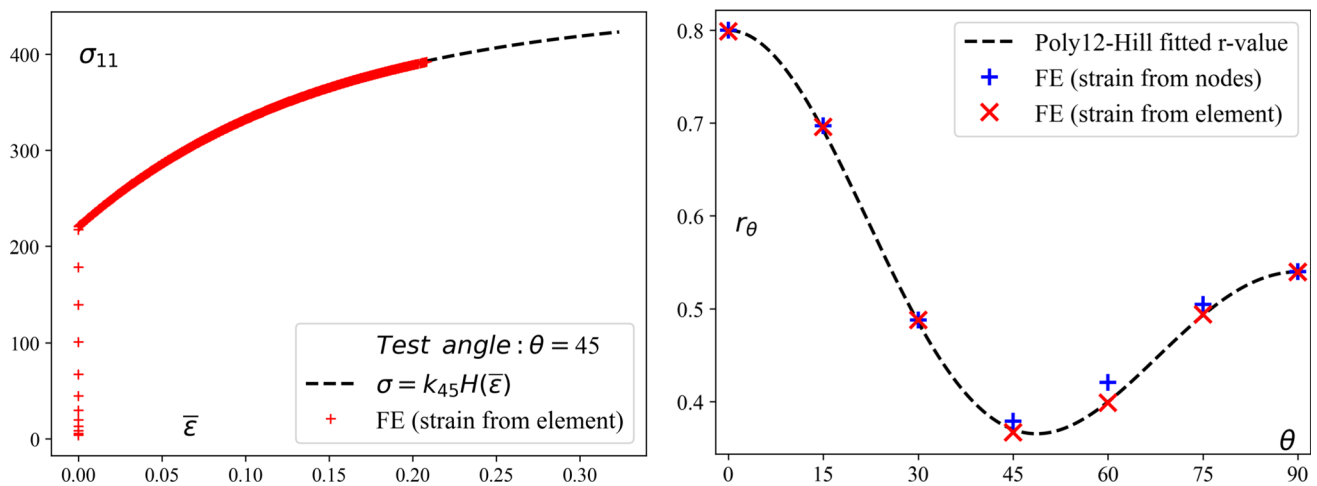
Fig. 4 FE-simulations testing the Poly12 clone of Hill'48 model (of AA6022-T4): the stress vs equivalent plastic strain curve of the $\theta = 45^o$ test (Left) and r-values at the end of each test (Right)

Table 1 Performance evaluation of PolyN based simulations of uniaxial tests

Model	r_0	r_{15}	r_{30}	r_{45}	r_{60}	r_{75}	r_{90}	Total run-time
Targets	**0.800**	**0.692**	**0.486**	**0.370**	**0.400**	**0.493**	**0.540**	*
Hill48-Abaqus	0.801	0.697	0.488	0.382	0.437	0.505	0.540	3924 | 3461
Hill48-UMAT	0.800	0.697	0.488	0.379	0.437	0.505	0.540	3739 | 3723
Poly4	0.800	0.697	0.488	0.379	0.451	0.505	0.540	3976 | 4110
Poly6	0.800	0.697	0.488	0.379	0.456	0.505	0.540	3936 | 4029
Poly8	0.800	0.697	0.488	0.379	0.452	0.505	0.540	3986 | 4105
Poly10	0.800	0.697	0.488	0.379	0.439	0.505	0.540	4010 | 4234
Poly12	0.800	0.697	0.488	0.379	0.421	0.505	0.540	4075 | 4316

The row 'Targets' stores samples from the theoretical Hill'48 fit shown in Fig. 2; Row 'Hill48-Abaqus' shows results from FE-simulation with the default Abaqus implementation; Row 'Hill48-UMAT' with Hill48 implemented by UMAT; The rest of the rows show results for PolyN clones of Hill'48. All r-values are inferred from nodes. Last column shows the sum of the run-times of all simulations in a row (Wallclock time, in seconds, as reported by Abaqus) in the format Mach-1 | Mach-2 (see Note below). All simulations were performed with the same time increment (One step, total time = 1, max. increment = 0.003). Simulations reported in this article were performed on a Linux machine (Intel-Xeon:3.1GHz, RAM:256GB) running Abaqus-2022 with Intel Fortran 19 compiler—referred to as Mach-1, and a Windows machine (Intel-Xeon:3.2GHz, RAM:32GB) running Abaqus-2014 with Intel Fortran 14—referred to as Mach-2. On both machines, Abaqus-Jobs were run with the parameter 'number of CPUs' set to 1

the second decimal place: For all practical purposes, the profiles are identical.

– The difference in runtimes, from Poly4 to Poly12 is small, if not negligible, for both uniaxial and cup-drawing tests.

and therefore, from a computational perspective, it makes little difference which PolyN model is used.

7 Cup-Drawing predictions and height profile analysis

The first systematic investigation of the mechanical properties of sheet metal by using cup-drawing experiments was performed by [31]. In honor of his pioneering work, cylin-drical cup-drawing is often referred to as the Swift cupping test. He identified many of the essential characteristics and parameters of the process (the stretching and drawing zones, the interplay between the hoop and radial stresses, the impact of lubricants and holding forces, etc), but one feature proved to be as elusive back then as it still is today. In Swift's own words (in the cited reference): *It must be admitted that the phenomenon of ear development is obscure. It may be that more exhaustive comparative tests will lead to some reliable correlation with mechanical properties, but before the phenomenon can be regarded as understood it will be necessary to explain also why ductility should vary in a directional manner, and why it should be greatest in different directions in different materials subjected to similar treatment.*
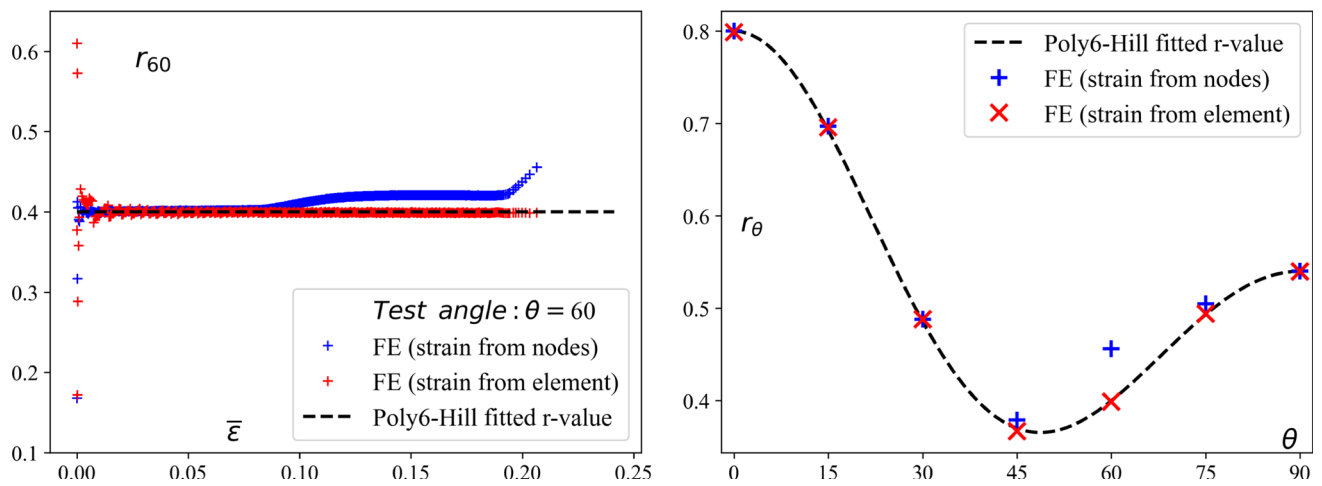
Fig. 5 FE-simulations testing the Poly6 clone of Hill'48 model (of AA6022-T4): The evolution of the r-value with equivalent plastic strain for the $\theta = 60^o$ test (Left) and all r-values at the end of each test (Right). The strains at integration points yield r-values (red markers) that match the expected theoretical targets. The strains inferred from node displacements (blue markers) are more sensitive to mesh instabilities

Fig. 6 *Left:* Schematics of the cylindrical deep-drawing operation (Note: All reported simulations were performed with fixed Holder-Die clearance). *Right:* Mesh used on (quarter) blank, consisting of 5246 shell S4R elements
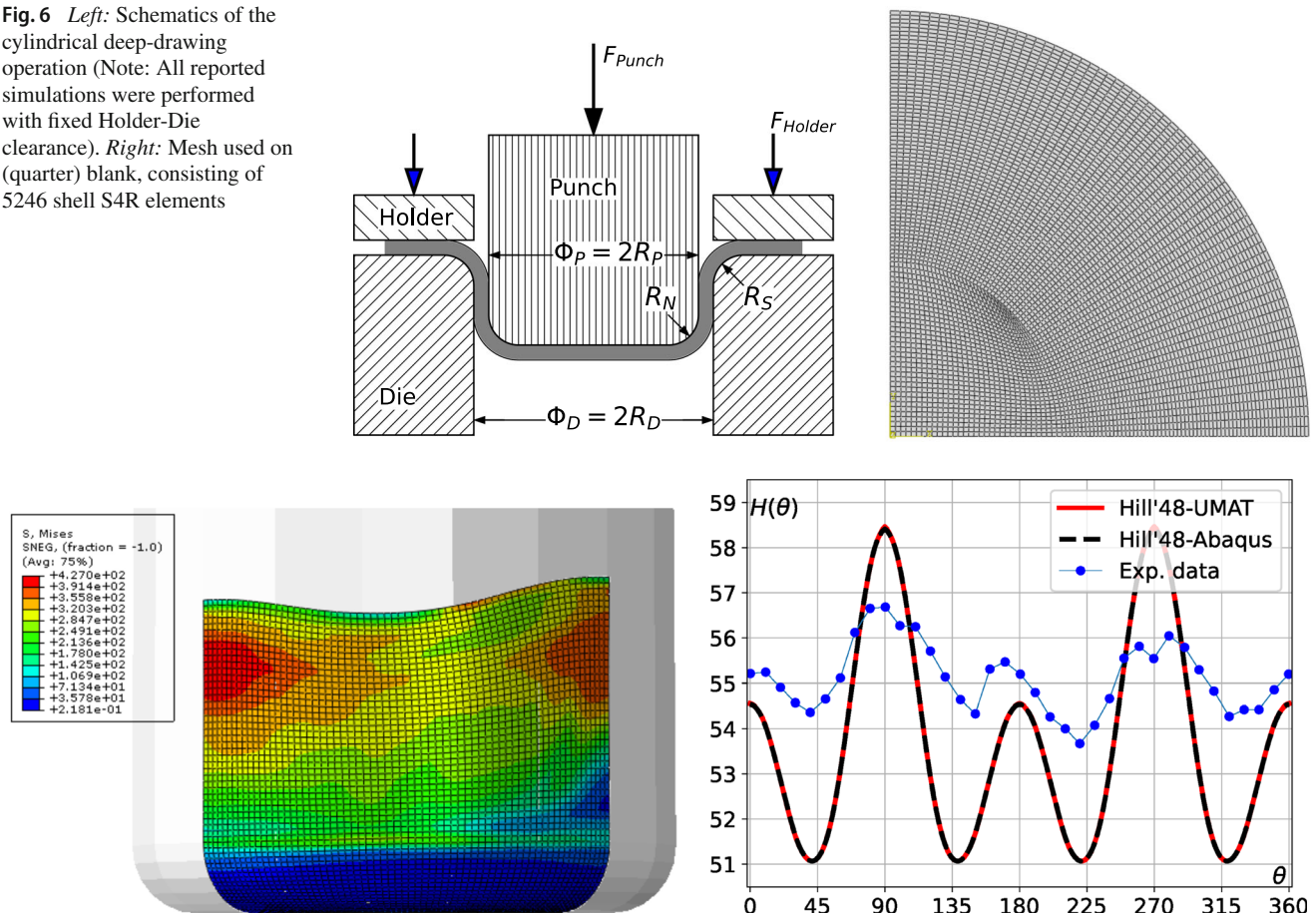
Fig. 7 *Left:* Hill'48 cup left on the punch at the end of a simulation (contact with the die is naturally removed by displacing the punch until the formed cup is completely out of the die hole). *Right:* FE cup profiles (extended by symmetry) and measured from actual experiments—digitized from [32]

Table 2 Performance evaluation of PolyN based simulations of cup-drawing tests

	Hill48-Abaqus	Hill48-UMAT	Poly4	Poly6	Poly8	Poly10	Poly12
Δ_H	0.0827	0	0.0002	0.0123	0.0196	0.0008	0.0102
Runtime	17399 20619	15979 20587	16673 ∗	16641 ∗	16843 ∗	16760 ∗	16921 ∗

Row Δ_H shows the norm difference calculated with Eq. (34) with the profile of Hill48-UMAT as reference H_R (units in millimeters). Row 'Runtime' shows the overall wallclock time, in seconds, as reported by Abaqus (See Note of Table-1). All simulations were performed with the same punch displacements and the same time increments (Four steps, total time of each step = 1, max. increment of the drawing step = 0.001). Numerical data (cup profiles) is available in the directory `CM_Data/AA6022_CupProfiles` of the code repository

The non-uniform cup height is essentially caused by the plastic anisotropy of the metal sheet [15]. Besides a simplified theory based on directional (uniaxial) r-values, e.g., [18], little is known about how this anisotropy is related or at least 'correlated' to the non-uniformity of the height profile. In this section, based on the concepts developed in Section-2, we present a numerical exploration of the problem. We use the new PolyN calibration algorithm to create models with tightly controlled features, with almost surgical precision, allowing us to discern a set of basic correlations between plastic properties and the predicted height profile. In the process, we also show the usefulness of PolyN cloning in assessing simulation results obtained with other yield functions.

7.1 PolyN profile predictions for AA6022-T4

We begin our analysis by showing profile predictions obtained with PolyN models of AA6022-T4 detailed in Appendix-C. The FE-setup is the same as in the previous section. However, some remarks on the setup itself, as described in [32], are necessary, in order to properly set expectations regarding FE-simulations results. Despite attempting near plane strain conditions on the flange area (fixed holder clearance, with only 0.04 of air between blank and tools), the authors of the cited work report significant wrinkling. This alters the expected stress state and the contact conditions during the drawing stage, both having a significant impact on the cup profile [22]. Also, since there are only 0.11mm of air between blank and tools on the die wall area, there is significant ironing in the final stage of the experiment. By a rough approximation, with most thickening taking place at the rim where $\epsilon_z \approx -\ln(\Phi_D/\Phi_B)$, the resulting final thickness at the rim, in the absence of ironing, would have been $t_B \exp(\epsilon_z) \approx 1.665$mm. Ironing smears out the extra material, partially filling the troughs, the overall effect being a taller cup and a reduction of the *relative height* of the ears (the difference between the maximum and minimum heights of the profile). A proper account of all these effects would require a full 3D analysis, which is beyond the scope of this work.

Figures 8 and 9 show the predicted profiles. We record here the main features:

(P_1) Of all PolyN profiles, Poly4 features the smallest local maxima, along RD and TD.
(P_2) Of all PolyN profiles, Poly12 features the highest local maxima, along RD and TD.
(P_3) Modulo small local differences, the Poly6, Poly8 and Poly10 profiles are nearly identical.

In addition, Fig. 9-Left, also shows (in dotted line) the digitized Yld2000-2D profile reported by [32] together with the profile (shown in dashed line) we obtained by using the Poly8 clone of the Yld2000-2D model of the cited reference, shown in Fig.4/Appendix-C. The difference between the two is most likely caused by the different simulation frameworks (here—implicit; cited work—explicit) but the most striking feature is conserved:

(P_4) The Yld2000-2D(Poly8) profile has the smallest relative height (approx 2.25mm) by comparison with all the other PolyN models (approx. 3.5mm for Poly4-Poly10, and approx. 4 mm for Poly12).

7.2 Further discussion: about the relationship between r-values and cup-profiles

The mainstream theory regarding the profile of a cylindrical deep-drawn cup asserts that both its topology and magnitude are mostly determined by the directional r-values of the material, e.g., [18]. While acceptable as a first approximation, the theory requires refinement. After all, if it were entirely true, all profiles reported so far, Hill'48 included, should have been nearly identical, since all are obtained using models with nearly identical (classical) r-values.

A more thorough understanding of the predicted PolyN profiles requires consideration of the biaxial nature of the stress state experienced by the blank during drawing and, in particular, of the generalized r-values corresponding to the drawing zone on the yield surface (i.e., for $q < 0$). These are shown in thin lines in Figs.4-9/Appendix-C and they correlate well with the $(P_1) - (P_4)$ profile features recorded above. To generalize, we consider a family $\mathcal{F} = \{f\}$ of models of a material with the property that all yield functions f predict the same uniaxial r-values and yield stresses. We assume that the drawing stresses are described by a range $q \in [-q_{max}, 0]$
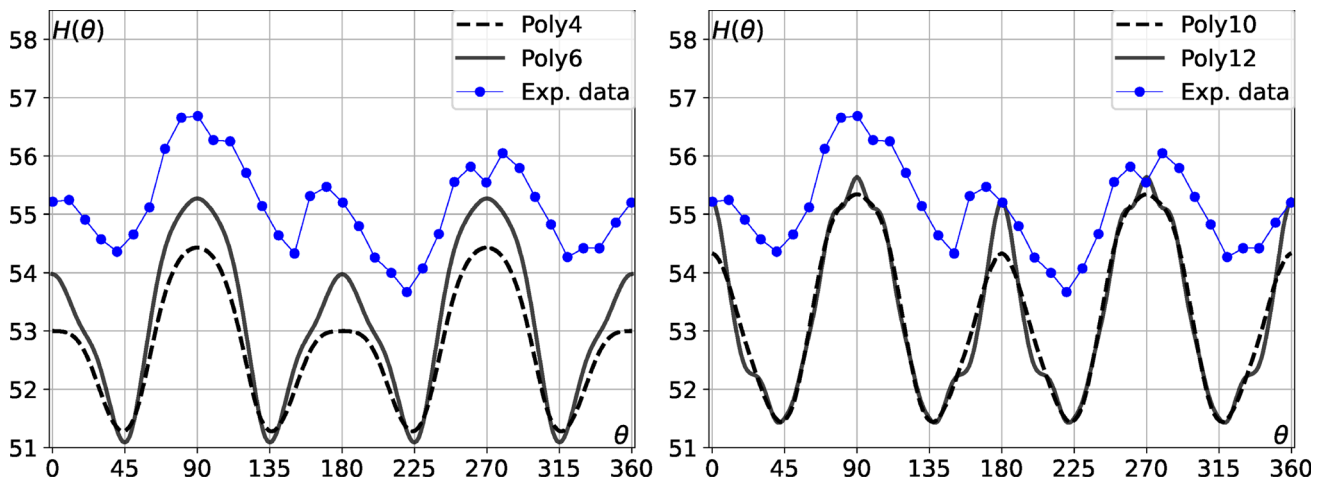
Fig. 8 AA6022-T4 predicted profiles by the PolyN models in Figs.5,6,8,9/Appendix-C
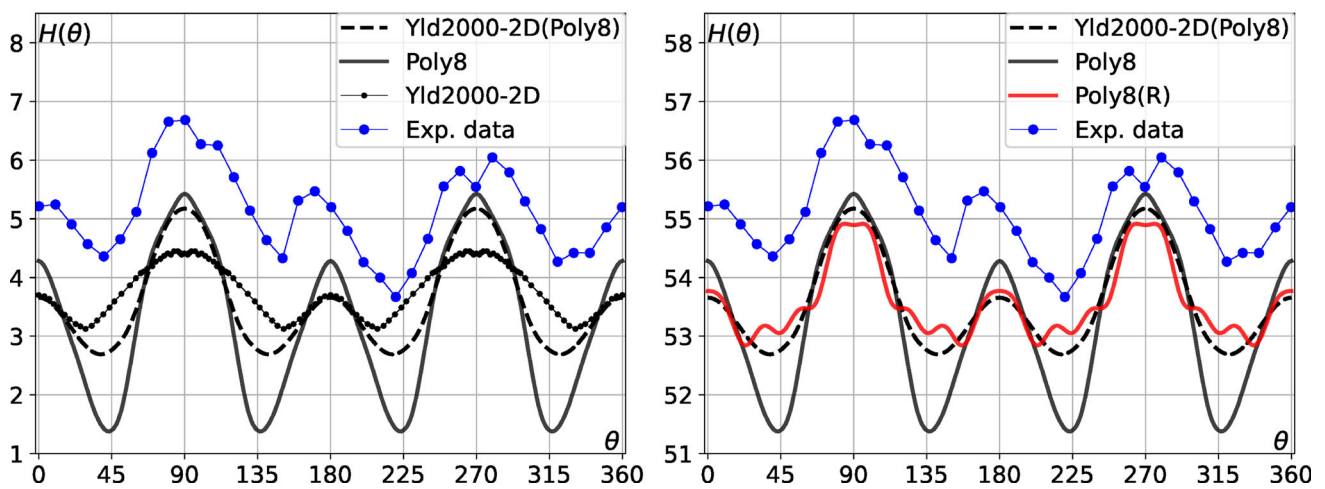

Fig. 9 AA6022-T4 predicted profiles. *Left:* by model Poly8(Fig.7/Appendix-C). *Right:* Poly8(R) / Figs. 10 and 11. Notes: 'Yld2000-2D' shows the profile digitized from [32] (predicted with Abaqus explicit); 'Yld2000-2D(Poly8)' shows the profile calculated here using the Poly8 clone of the Yld2000-2D model and Abaqus-implicit

and denote by $r_f = r_f(q, \theta)$ the r-values predicted by a function $f \in \mathcal{F}$, for $q \in [-q_{max}, 0]$, and by $\mathcal{H} = \{H_f\}$ the set of cup height profiles predicted by $\mathcal{F}$. We assert the following correlations:

(C_1) If $f_1, f_2 \in \mathcal{F}$ satisfy $r_{f_1} \le r_{f_2}$ then $H_{f_1} \le H_{f_2}$
(C_2) If $f_1, f_2 \in \mathcal{F}$ satisfy $r_{f_1} = r_{f_2}$ then $H_{f_1} = H_{f_2}$
(C_3) The variation $VH_f = \max(H_f) - \min(H_f)$ is controlled by $Vr_f(q) = \max\limits_{\theta \in [0, \pi/2]} (r_f) - \min\limits_{\theta \in [0, \pi/2]} (r_f)$

Correlation C_1 should be nearly obvious, since it extends a similar correlation observed for classical (uniaxial) r-values. C_2 asserts that two models with the same uniaxial properties may not predict the same cup profile. This is confirmed by all simulations shown here. To further illustrate C_3, we constructed a second Poly8 model of AA6022T4 by augmenting the dataset in Table 1/Appendix-C with the following set

of biaxial r-values: $r(q, 0^o) = 2.5$, $r(q, 15^o) = 2.1$, $r(q, 30^o) = 1.7$, $r(q, 45^o) = 1.7$, $r(q, 60^o) = 1.7$, $r(q, 75^o) = 1.8$, $r(q, 90^o) = 1.9$, where $q = -0.2$. In essence, we modified the biaxial r-values of the Poly8 model in Fig.7/Appendix-C to mimic the variation featured by the clone Yld2000-2D(Poly8) in Fig.4/Appendix-C. The resulting Poly8 model, referred to as Poly8(R), is shown in Figs. 10 and 11, and the corresponding height profile in Fig. 9-Right. Correlation C_3 is confirmed: By leveling up the r-values for $q < 0$, we managed to reduce significantly the relative height (which is approx. 2 mm for the Poly8(R) predicted cup).

7.3 AA6016-T4: Ear swapping, Oscillations

An important prediction of the classical theory based on uniaxial r-values regards the so-called *earing trend*. In the particular case of profiles with four ears (maxima) along
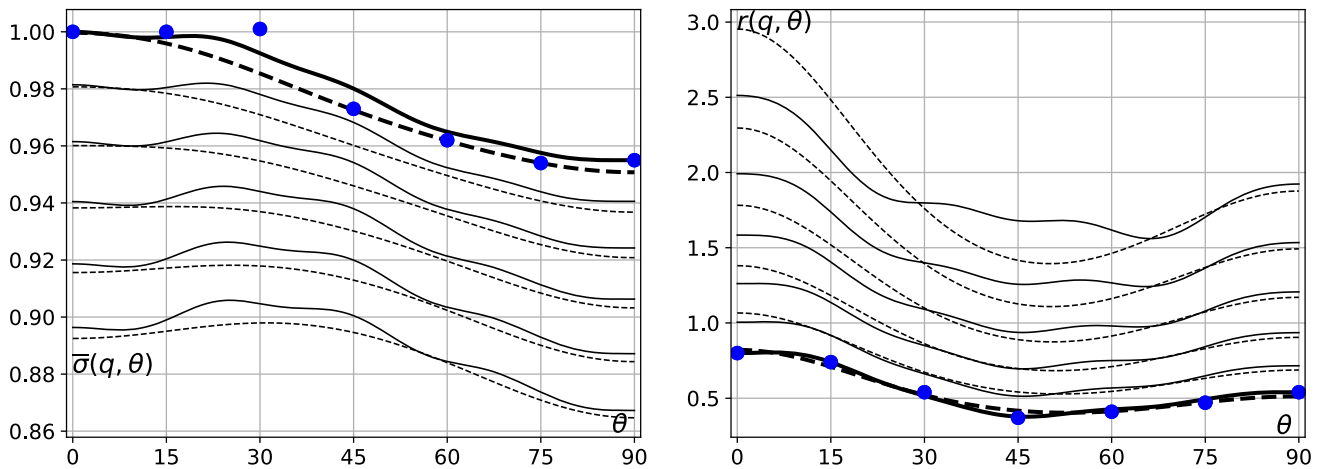
Fig. 10 Poly8(R) model (solid lines) and Yld2000-2D(Poly8)-clone of the model reported in [32] (shown here with dashed lines) of AA6022-T4. Circle markers represent uniaxial data; Thick line—Uniaxial ($q = 0$); Thin lines - Biaxial($0 > q > -0.25$). *Left:* Yield stress. *Right:* r-values
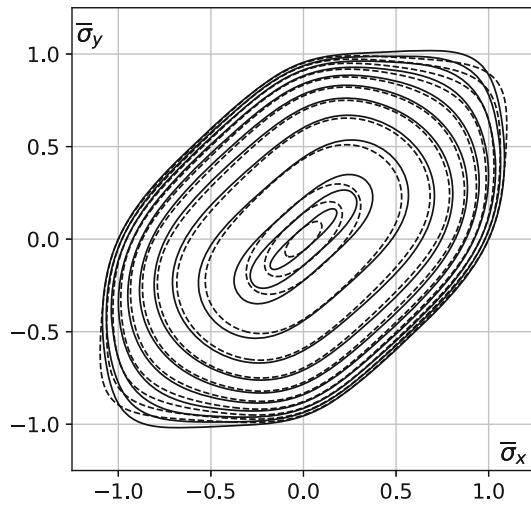
Fig. 11 $\sigma_{xy} = const$ sections through the yield surfaces of the two models in Fig. 10: Poly8(R)—solid; Yld2000-2D(Poly8)—dashed. The two models are similar in the drawing zone but differ significantly near the balanced-biaxial stress state (discussion in Appendix-C)

RD and TD, it asserts the following implications [18]: If $r_0 \leq r_{90}$ then $H(0°) \geq H(90°)$; and its reverse, if $r_0 \geq r_{90}$ then $H(0°) \leq H(90°)$. This trend is indeed observed in cup drawing experiments for many materials, AA6022-T4 serving as illustration.

A recent cup-drawing experiment performed with AA6016-T4 appears to contradict the above rule [12]. The cited reference reports two sets of mechanical characterizations, discussed in some detail in Appendix-D of this article. In one characterization, referred to as TUAT, the uniaxial r-values of the sheet satisfy the inequality $r_0 < r_{90}$, whereas in the other, referred to as UA, they satisfy the opposite $r_0 > r_{90}$. Both inequalities appear to hold by a non-negligible margin, greater than the expected variations caused by heterogene-

ity. On the other hand, the outcome of the deep-drawing experiment is a cup height profile featuring the inequality $H_0 < H_{90}$, by a significant margin also, greater than the expected variations caused by heterogeneity and blank centering. According to the invoked theory of the earing trend, this is in obvious conflict with the TUAT characterization. The question then is whether a yield surface model of the TUAT data can predict the experimentally observed profile, thus effectively featuring what may be called *ear swapping*, i.e., an earing trend opposite to the one expected based on the classical theory of earing.

Before answering, it is instructive to briefly discuss two particular models, Caz2018-Ort and FACET, reported in [12], the reader being referred to Appendix-D for further analysis of other models reported in the cited work. The Caz2018-Ort model was constructed based on the UA-data and, since it predicts the uniaxial r-values correctly, Fig. 12-Right, the predicted[6] cup profile follows the expected earing trend as discussed above, Fig. 15-Left. However, it also overestimates the experimentally observed profile quite significantly. This is unexpected since our plane stress simulation does not account for ironing effects (and hence an underestimate of the cup-profile would have been expected instead). A closer inspection of Fig. 12-Right reveals that, by comparison with all AA6016-models discussed here (and in Appendix-D), this model features the largest generalized r-values (for $q < 0$) and hence, in agreement with correlation C_1, the corresponding profile prediction is expected to be the tallest. A similar

---

6 For all simulations reported in this subsection we used the corresponding friction and hardening data in Tables-10,32 of [12]. Also, with reference to Fig. 6 and Eq. (33): $\Phi_D = 62.4$, $\Phi_P = 60.0$, $R_N = 5.0$, $R_S = 10.0$, $\Phi_B = 107.5$ $t_B = 1.0$. Finally, we recall that for simulations with classical shell elements the thickness of the blank has no relevance (besides the integration points used for calculating the response to bending).
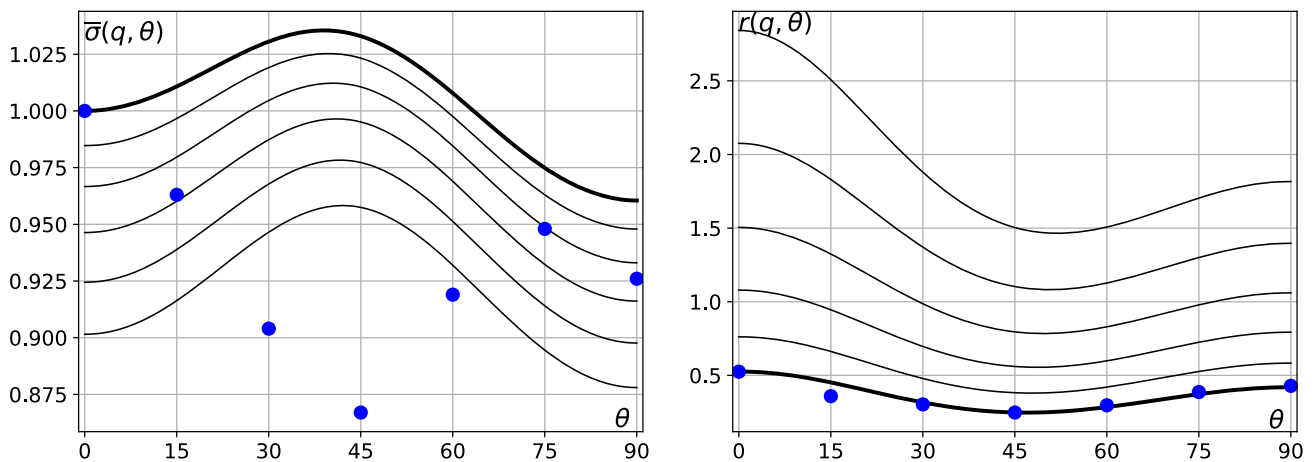
Fig. 12 **Poly8** clone of the Caz2018-Ort model of AA6016-T4(UA), where dots represent uniaxial data; Thick line - Uniaxial ($q = 0$); Thin lines—Biaxial($0 > q > -0.25$). *Left:* Yield stress; *Right:* r-values. Corresponding biaxial curves are shown in Fig. 13-Left

Fig. 13 $\sigma_{xy} = const$ sections through the yield surfaces of several models of AA6016T4. *Left:* Caz2018-Ort with directional properties in Fig. 12. *Right:* FACET-R (solid) and FACET (dashed) corresponding to the two models in Fig. 14
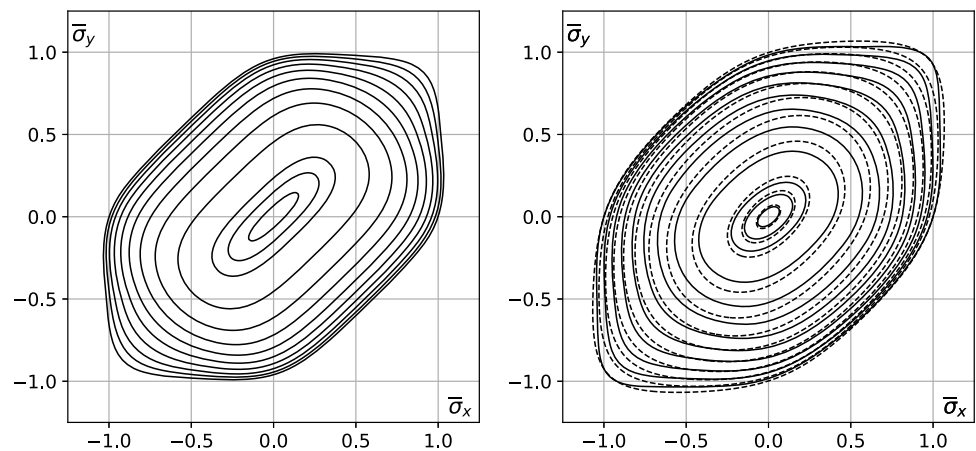
overestimate of the cup profile is observed in many other plane stress simulations, e.g., for the Yld2000-2d and Yld91 models reported in [21] and [40], respectively, its most likely cause being too large generalized r-values ($q < 0$).

On the other hand, the FACET model, constructed using the TUAT data, was able to predict ear swapping by offsetting the initial position of the blank by -0.3mm along RD. For an intrinsic assessment, without blank offset, we performed a simulation using the Poly8 clone of the this model (Appendix-E), in a fully orthotropic setup (quarter blank subject to symmetric boundary conditions). The result is shown in Fig. 15-Left: With $H(0°) = 34.33$mm and $H(90°) = 34.37$mm, the ear swap featured by the fully orthotropic FACET predicted profile is negligible (≤ 0.05mm) and for all practical purposes the ears have equal height. This profile symmetry correlates well with the nearly symmetrical distribution of r-values and yield stresses featured by the FACET model, Fig. 14.

Interestingly enough, both Caz2018-Ort and FACET models predict the corresponding uniaxial r-values correctly but are far from adequate in their predictions of the directional

stresses, Fig. 12,14-Left, and hence our next question. Would it be possible to improve the profile prediction of the FACET model (since our main interest is in the TUAT data) by improving its fit of the directional yield stress ? To answer this we aggregated the uniaxial TUAT yield stresses with the r-values predicted by the FACET model, i.e., $r(q, \theta)$ for $q \in \{0, -0.05, -0.1, -0.15, -0.2\}$ and $\theta \in \{k\pi/24 \,|\, k = 0, \ldots, 12\}$, into an input data set. The resulting Poly8 model, referred to as FACET-R and shown in solid line in Fig. 14, has practically the same r-values as FACET and a significantly improved fit of the directional yield stresses. And yet, the cup profile predicted by this model, Fig. 15-Right, is most surprising: With eight ears located in anti-phase with the actual profile (it has troughs/minima along RD and TD, instead of ears/maxima). To explain this we recall that the theory based on classical r-values correlates the ears with the local maxima of the uniaxial r-values. More generally, local maxima of the generalized r-values have also been linked to profile ears—at least in theory/simulation [28]. Since the *same* yield surface model may predict different cup profile topologies in conjunction with different element technologies [40], it
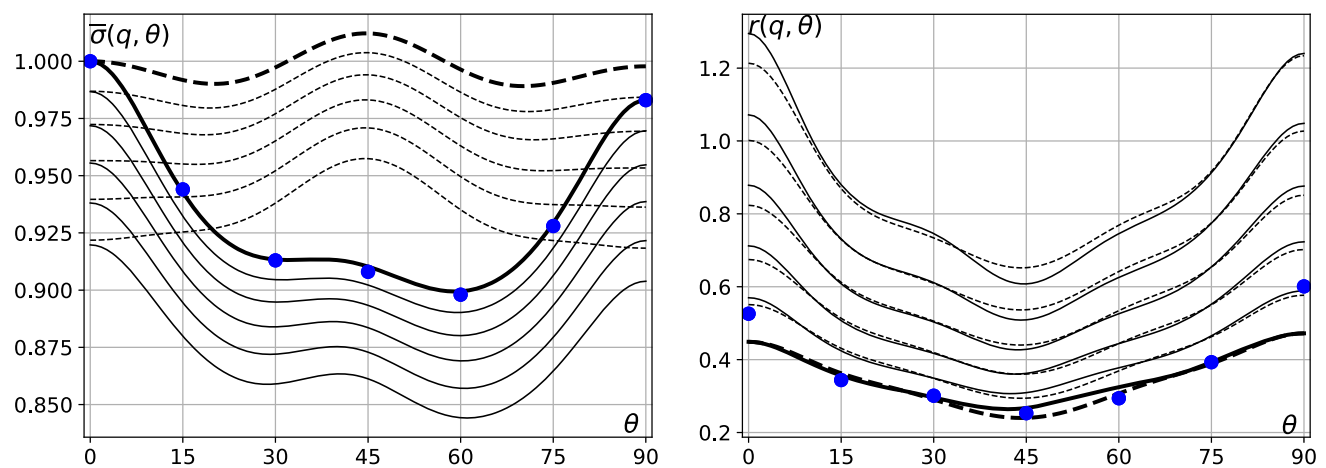
Fig. 14 Yield stresses (Left) and r-values (Right) of two Poly8 models of AA6016T4(TUAT). Markers represent uniaxial data. Thick line—Uniaxial ($q = 0$); Thin lines—Biaxial($0 > q > -0.25$). *Dashed:* Poly8 clone of the FACET model reported in [12], also referred to as FACET(Poly8). *Solid line:* the FACET-R model, obtained by fitting the r-values predicted by the FACET-model and the actual TUAT yield stress data. Corresponding biaxial curves are shown in Fig. 13-Right
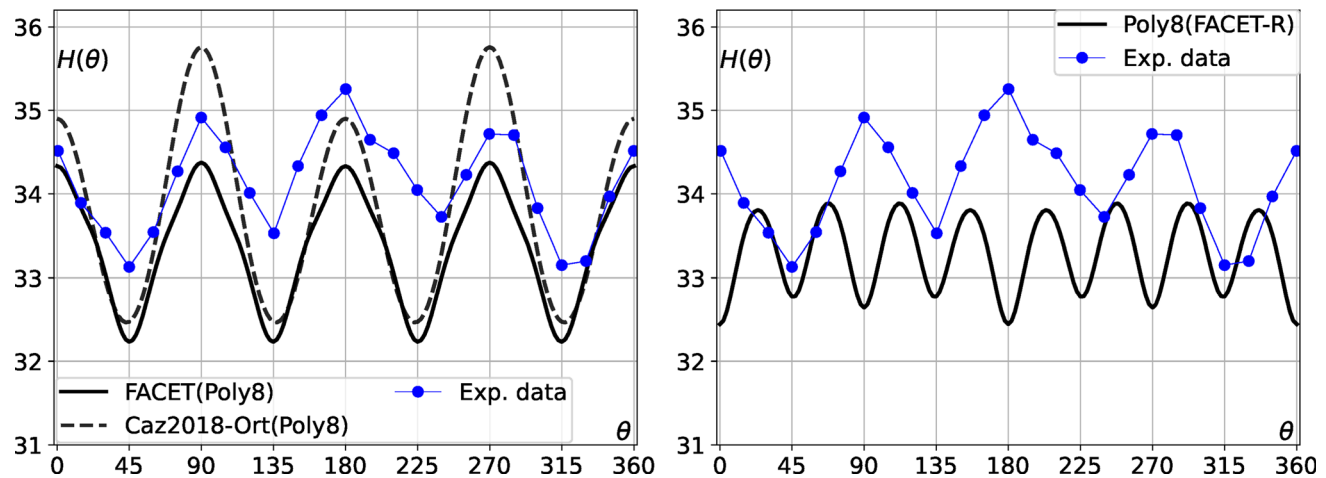
Fig. 15 *Left:* FACET(Poly8) prediction without offset, model in Fig. 14, and Caz2018-Ort(Poly8) prediction. The Caz2018-Ort profile reported in [12] was obtained using 3D elements and a different contact definition. Here, to facilitate a better comparison we recalculated it with the shell-based setup used in this work and using the Poly8 clone of the Caz2018-Ort model, Fig. 12. *Right:* Profile prediction of the Poly8 model of the FACET r-values combined with the actual yield stresses (TUAT), i.e., model FACET-R shown with solid line in Fig. 14

appears that their manifestation is strongly influenced by the predicted stress field (during the drawing stage). Such local maxima, or even peculiar inflection points, are at the origin of many profile *oscillations* observed in simulations. The latter are indeed featured by the Poly12 model in Fig.9/Appendix-C and reflected on the corresponding profile in Fig. 8-Right; They are also featured by the Poly8(R) model in Fig. 10 and reflected on the corresponding profile in Fig. 9-Right. In the present case, however, such variations are too small to explain the large ears featured by the FACET-R profile near the $\theta = 60°$ and $30°$ locations. Rather, these locations are activated and then favored by the two corresponding local minima featured by the yield stress near $\theta = 30°$ and $60°$, Fig. 14-Left. More generally, we conjecture that:

(C_4) The potential ear locations predicted by a yield surface model are in the set $\mathcal{S}_C$ of critical points of the drawing stresses $\sigma(q, \theta)$ for $q \leq 0$. Ears develop at those locations in $\mathcal{S}_C$ where the drawing r-values $r(q, \theta)$ for $q \leq 0$ are greater than a critical threshold.

This conjecture amends and extends a Lemma of Hill [15], Ch-12, page 331, stating the following relationship between the predicted uniaxial yield stresses and predicted profile: *the ears and hollows form where the tangents to the rim are in the directions of stationary yield stresses.*

(C_4) implies a strong coupling between the directional yield stresses and r-values. To further test it, we constructed two models of the UA data, UA-1 and UA-2, shown in Fig. 16.
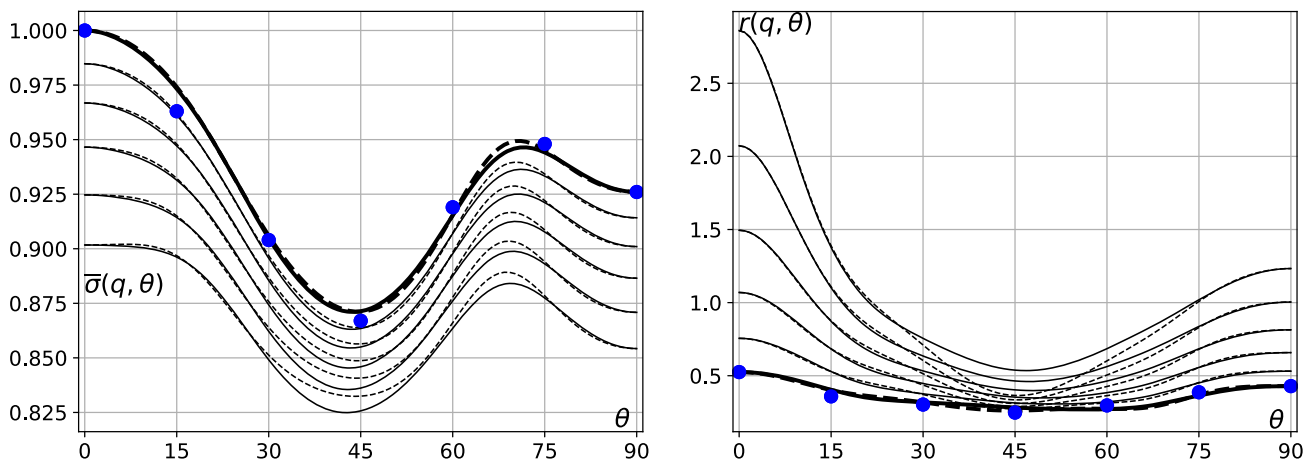
Fig. 16 Two **Poly8** models (UA-1: solid; UA-2: dashed) of the AA6016T4(UA) data set, where dots represent uniaxial data; Thick line—Uniaxial ($q = 0$); Thin lines - Biaxial($0 > q > -0.25$). *Left:* Yield stress; *Right:* r-values. Corresponding biaxial curves are shown in Fig. 17-Left

Fig. 17 $\sigma_{xy} = const$ sections through the yield surfaces of several models of AA6016T4. *Left:* UA-1(solid) and UA-2(dahsed) shown in Fig. 16. *Right:* Poly8 model of the TUAT data shown in Fig. 18
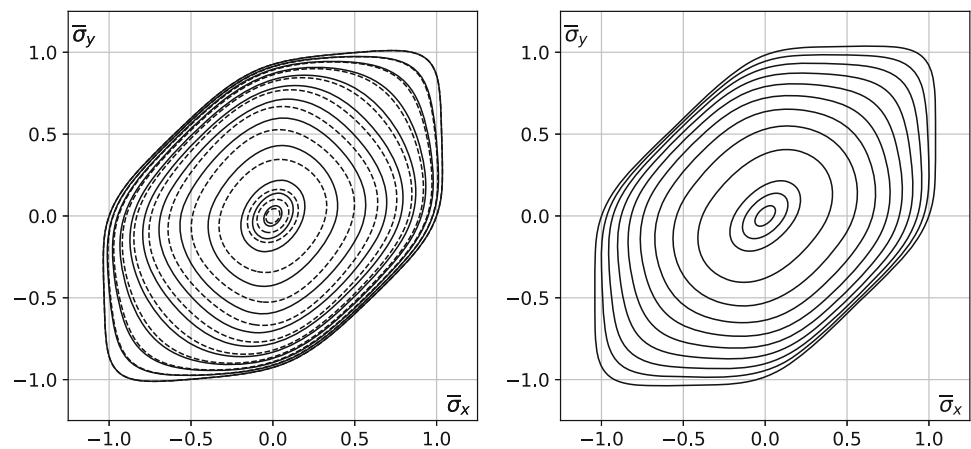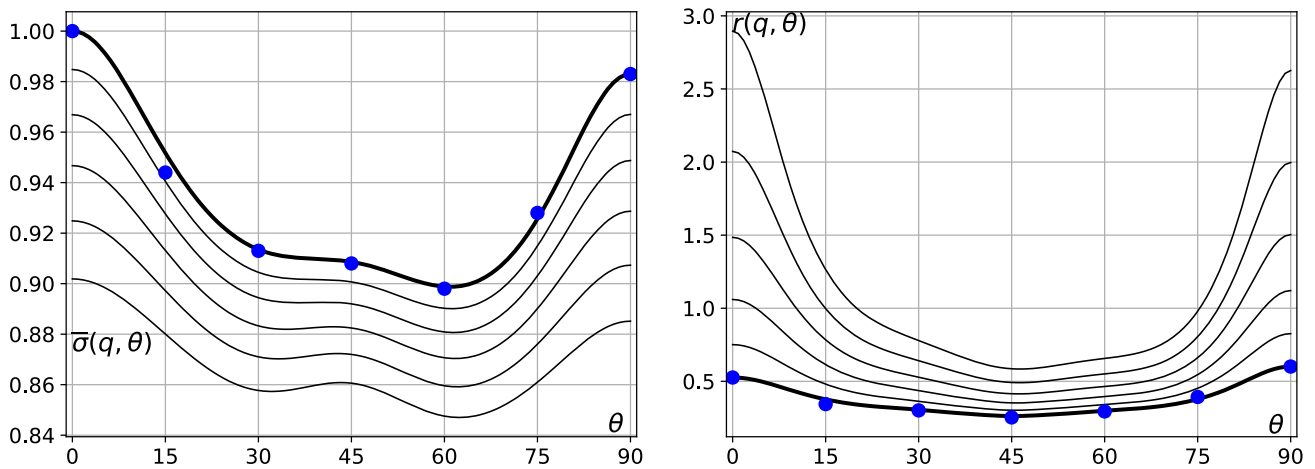

The corresponding cup profiles are shown in Fig. 19-Left (Obtained using the same hardening and friction parameters as used for Caz2018-Ort). For all practical purposes, the two models feature identical (uniaxial) directional properties. The UA-2 model (dashed) is a locally modified version of UA-1, specifically designed to have smaller (generalized) r-values in the vicinity of the $\theta = 45°$ minimum of the (generalized) directional stresses, in order to provide a sharper test for the (C_4)-conjecture. This is indeed reflected in the corresponding height profiles: The UA-1 profile has four additional small ears at $45° + k\pi/2$, $k = 0, 1, 2, 3$, while UA-2 features the correct topology and trend.

Finally, returning to our question regarding the TUAT data and the earing trend, it should now be clear that a reversal of the latter is possible only *if the generalized r-values reverse their trend also*, i.e., $r(q = -0.05, \theta = 0°) > r(q = 0, \theta = 90°)$, $r(q = -0.1, \theta = 0°) > r(q = -0.05, \theta = 90°)$, etc. At the same time, the incorrect profile predicted by the Poly8(FACET-R) model, which was obtained by combining the *symmetrical* distribution of r-values of the FACET-model with the actual (experimen-

tally measured) directional stresses, indicates that a strong correlation exists between the actual uniaxial stresses and r-values. Based on these observations we constructed a Poly8 model of the TUAT data in two steps as follows. In the first step, we generated a basic model with the help of additional samples from the top of a Hill'48 model (Section-3/Input data); In the second step, we extracted the stresses of the basic model corresponding to $q < 0$ and augmented the input data, over a few trial-and-error sub-steps, with generalized r-values $r(q < 0, \theta)$ featuring the opposite trend of their uniaxial counterparts, i.e., we increased/decreased as much as possible, without affecting the fit of the uniaxial properties, $r(q < 0, \theta = 0)$ and $r(q < 0, \theta = 90°)$, respectively. The resulting model of the TUAT data is shown in Fig. 18 and the corresponding profile (simulated with the same hardening and friction parameters as used for FACET) in Fig. 19-Right. The predicted profile features the ear swap $H(0°) = 34.31\text{mm} < H(90°) = 34.59\text{mm}$, thus providing a positive answer to our question.

Fig. 18 **Poly8** model of the TUAT data set, where dots represent uniaxial data; Thick line—Uniaxial ($q = 0$); Thin lines—Biaxial($0 > q > -0.25$). *Left:* Yield stress; *Right:* r-values. Corresponding biaxial curves are shown in Fig. 17-Right
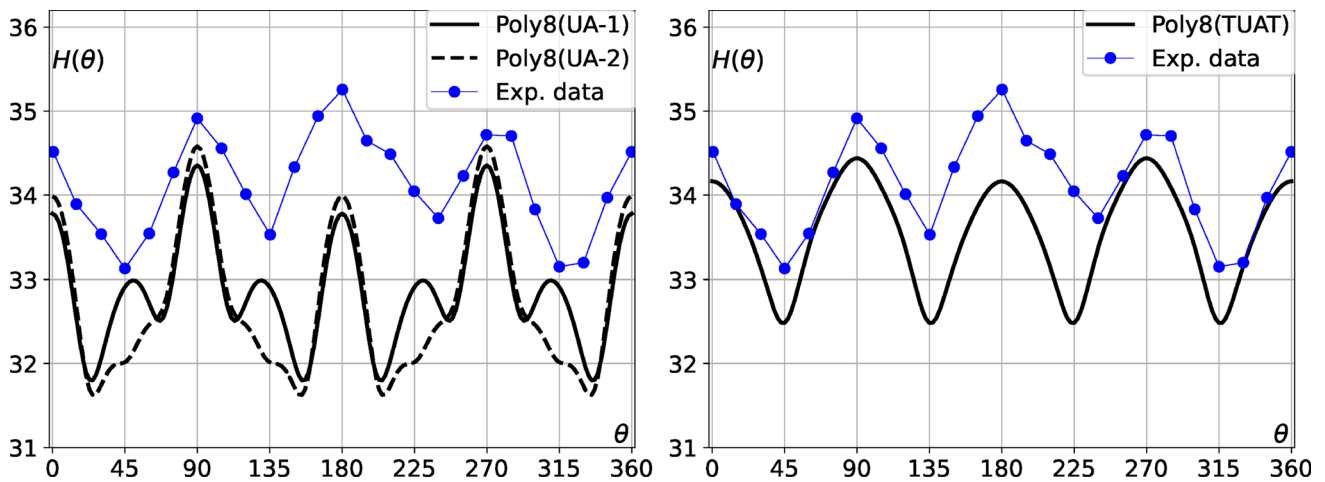
Fig. 19 *Left:* Profile predictions of the two Poly8 models of the UA data, Fig. 16. *Right:* Profile prediction of the Poly8 model of the TUAT data, Fig. 18

8 Conclusions

High order homogeneous polynomials are powerful modeling tools being capable of rendering a wide variety of geometrical shapes. In metal plasticity they were first considered by Hill [15]/Ch.-12, in essentially the same general form as employed here. However, their use in practical applications has been hindered by the lack of a reliable and user-friendly calibration scheme capable of delivering convex models of the yield surface. Here we showed a general calibration procedure with several distinctive features:

- Applicable to virtually any PolyN of practical interest (demonstrated here for $N \in \{4, 6, 8, 10, 12\}$).
- Capable of handling convexity via linear constraints (by contrast with the natural formulation where the constraints are quadratic) and hence amenable to a complete

automation of the calibration process (as shown by the provided code).
- Capable of handling arbitrary data: From the traditional data set based on the uniaxial properties of the sheet (as shown here for AA6022-T4/App-C), to data generated by virtual testing (such as the FACET model of AA6016-T4) or by sampling other non-polynomial yield functions (such as the non-integer exponent Yld2000-2d model/App-D), and finally, to any heuristic combination of data (such as FACET-R), even inferred from the outcome of the deep-drawing experiment itself (such as Poly8-R and Poly8(TUAT)).

At the same time, high order polynomials pose new implementation challenges, since in canonical form they are computationally expensive and prone to precision loss. Here we showed a general Horner-scheme for their evaluation,

demonstrated for $N \leq 12$ to yield simulation run-times similar to those of Hill'48 (for simple uniaxial tests and cylindrical deep-drawing). Furthermore, the generality of the scheme allows PolyN to be implemented into a single constitutive routine for arbitrary N, thus obtaining an effective simulation tool covering a broad spectrum of yield functions (as shown by the provided UMAT).

Finally, the fitting capabilities of the calibration procedure were tested on the modeling of two aluminum alloys, AA6022-T4 and AA6016-T4, and then on the prediction of the corresponding deep-drawn cup profiles via finite element simulations. The calibration algorithm was shown to be capable of generating multiple models of the same material, with fixed uniaxial properties, while controlling other areas of the yield surface, such as the drawing zone. This allowed us to explore in unprecedented detail the relationship between predicted cup profiles and yield surface models. We observed several correlations that can be used in practice to infer the drawing zone of a yield surface from experimental cup-profiles. This effectively opens the possibility of including the Swift cupping test in the list of mechanical tests that are used to calibrate yield surface models.

Data availability All supporting code is made public at: https://github.com/stefanSCS/PolyN. Numerical data (parameters and cup height profiles) for all models and deep-drawing simulations reported here is available in the `CM_Data` sub-directory of the repository.

References

1. Banabic D, Comsa DS, Sester M, Selig M, Kubli W, Mattiasson K, Sigvant M (2008) Influence of constitutive equations on the accuracy of prediction in sheet metal forming simulation. Numisheet, September 1–5, 2008-Interlaken, Switzerland

2. Barlat F, Lian J (1989) Plastic behavior and stretchability of sheet metals. Part 1: a yield function for orthotropic sheets under plane stress conditions. Int J Plast 5:51–66

3. Barlat F, Brem JC, Yoon J-W, Chung K, Dick RE, Lege DJ, Pourboghrat F, Choi S-H, Chu E (2003) Plane stress yield function for aluminum alloy sheets? Part 1: theory. Int J Plast 19:1297–1319

4. Barlat F, Aretz H, Yoon J-W, Karabin ME, Brem JC, Dick RE (2005) Linear transformation based anisotropic yield function. Int J Plast 21:1009–1039

5. Biswas A, Kalidindi SR, Hartmaier A (2022) A hybrid approach for the efficient computation of polycrystalline yield loci with the accuracy of the crystal plasticity finite element method. Model Simul Mater Sci Eng 30:025015

6. Boehler JP (1987) Application of tensors functions in solids mechanics, CISM Courses and Lectures, vol 292. Springer, Berlin

7. Boyd S, Vandenberghe L (2004) Convex optimization. Cambridge University Press. Python code at https://cvxopt.org/

8. Bron F, Besson J (2004) A yield function for anisotropic materials. Application to aluminum alloys. Int J Plast 20:937–963

9. Belytschko T, Liu WK, Moran B (2006) Nonlinear finite elements for continua and structures. Wiley, Chichester, UK

10. Gawad J, Van Bael A, Eyckens P, Samaey G, Van Houtte P, Roose D (2013) Hierarchical multi-scale modeling of texture induced plastic anisotropy in sheet forming. Comput Mater Sci 66:65–83

11. Gotoh M (1977) A theory of plastic anisotropy based on a yield function of fourth order (plane stress): part I and II. Int J Mech Sci 19:505

12. Habraken AM, Aksen TA, Alves JL, Amaral RL, Betaieb E, Chandola N, Corallo L, Cruz DJ, Duchêne L, Engel B, Esener E, Firat M, Sörensen PF, Lopez JG, Ghiabakloo H, Kestens AI, Lian J, Lingam R, Liu W, Ma J, Menezes LF, Minh TN, Miranda SS, Neto DM, Pereira AFG, Prates PA, Reuter J, Baudard BR, Ulloa CR, Sener B, Shen F, Van Bael A, Verleysen P, Barlat F, Cazacu O, Kuwabara T, Lopes A, Oliveira MC, Santos AD, Vincze G (2022) Analysis of ESAFORM 2021 cup drawing benchmark of an Al alloy, critical factors for accuracy and efficiency of FE simulations. Int J Mater Form 15:61

13. Hershey AV (1954) The plasticity of anisotropic aggregate of anisotropic face centered cubic crystals. J Appl Mech 21:241–249

14. Hill R (1948) A theory of the yielding and plastic flow of anisotropic metals. Proc R Soc Lond Ser A 193A(1033):281–297

15. Hill R (1950) The mathematical theory of plasticity. Clarendon Press, Oxford, UK

16. Hill R (1967) The essential structure of constitutive laws for metal composites and polycrystals. J Mech Phys Solids 15:79–95

17. Hosford WF (1972) A generalized isotropic yield criterion. J Appl Mech 39:607–609

18. Hosford WH, Caddell RM (1993) Metal forming: mechanics and metallurgy (2nd edn). PTR Prentice Hall, Upper Saddle River, NJ, USA. Ch-14

19. Karafillis AP, Boyce MC (1993) A general anisotropic yield criterion using bounds and a transformation weighting tensor. J Mech Phys Solids 41:1859–1886

20. Kocks UF, Tomé CN, Wenk H-R (2000) Texture and anisotropy: preferred orientations in polycrystals and their effect on material properties. Cambridge University Press, Cambridge

21. Liu W, Huang J, Pang Y, Zhu K, Li S, Ma J (2023) Multi-scale modelling of evolving plastic anisotropy during Al-alloy sheet forming. Int J Mech Sci 247:108168

22. Neto DM, Oliveira MC, Dick RE, Alves JL, Menezes LF (2022) Non-uniform effect of the contact conditions on the earing profile in cylindrical cups of anisotropic materials. Key Eng Mater 926:1188–1194

23. Rice JR (1971) Inelastic constitutive relations for solids: an internal-variable theory and its application to metal plasticity. J Mech Phys Solids 19:433–455

24. Roters F, Diehl M, Shanthraj P, Eisenlohr P, Reuber C, Wong SL, Maiti T, Ebrahimi A, Hochrainer T, Fabritius H-O, Nikolov S, Friak M, Fujita N, Grilli N, Janssens KGF, Jia N, Kok PJJ, Ma D, Meier F, Werner E, Stricker M, Weygand D, Raabe D (2019) DAMASK: the Dusseldorf advanced material simulation kit for modeling multiphysics crystal plasticity, thermal, and damage phenomena from the single crystal up to the component scale. Comput Mater Sci 158:420–478

25. Simo JC, Hughes TJR (2000) Computational inelasticity. Springer-Verlag, New York

26. Soare SC, Yoon J-W, Cazacu O (2008) On the use of homogeneous polynomials to develop anisotropic yield functions with applications to sheet forming. Int J Plast 24:915–944

27. Soare SC, Barlat F (2010) Convex polynomial yield functions. J Mech Phys Solids 58:1804–1818

28. Soare SC, Barlat F (2011) A study of the Yld 2004 yield function and one extension in polynomial form: a new implementation algo-

rithm, modeling range, and earing predictions for aluminum alloy sheets. Eur J Mech A/Solids 30:807–819

29. Soare SC (2022) A parameter identification scheme for the orthotropic Poly6 yield function satisfying the convexity condition. Eur J Mech A/Solids 92:104467

30. Soare SC (2023) Bezier5YS and SHYqp: a general framework for generating data and for modeling symmetric and asymmetric orthotropic yield surfaces. Eur J Mech A/Solids 97:104781

31. Swift HW (1939) Drawing tests for sheet metal. Proc Inst Automob Eng 34:361

32. Tian H, Brownell B, Baral M, Korkolis YP (2017) Earing in cup-drawing of anisotropic Al-6022-T4 sheets. Int J Mater Form 10:329–343

33. Tong W (2018) On the certification of positive and convex Gotoh's fourth-order yield function. IOP Conf Ser J Phys 1063:012093

34. Tong W (2018) Calibration of a complete homogeneous polynomial yield function of six degrees for modeling orthotropic steel sheets. Acta Mech 229:2495–2519

35. Van Houtte P, Clarke AP, Saimoto S (1993) A quantitative analysis of earing during deep drawing. In: Morris JG, Westerman EJ, Morris PL (eds) Aluminum alloys for packaging. TMS, Warrendale, PA, pp 261–273

36. Van Houtte P, Yerra SK, Van Bael A (2009) The facet method: a hierarchical multilevel modelling scheme for anisotropic convex plastic potentials. Int J Plast 25:332–360

37. Varjú PP (2007) Approximation by homogeneous polynomials. Constr Approx 26:317–337

38. Vegter H, Boogaard AH (2006) A plane stress yield function for anisotropic sheet material by interpolation of biaxial stress states. Int J Plast 22:557–580

39. Yoshida F, Hamasaki H, Umeori T (2013) A user-friendly 3D yield function to describe anisotropy of steel sheets. Int J Plast 45:119–139

40. Younas N, Chalal H, Abed-Meraim F (2020) Finite element simulation of sheet metal forming processes using non-quadratic anisotropic plasticity models and solid-shell finite elements. Procedia Manuf 47:1416–1423

41. Zhang K, Holmedal B, Hopperstad OS, Dumoulin S, Gawad J, Van Bael A, Van Houtte P (2015) Multi-level modelling of mechanical anisotropy of commercial pure aluminium plate: crystal plasticity models, advanced yield functions and parameter identification. Int J Plast 66:3–30